The Thesis Committee for Edwin Peng
Certifies that this is the approved version of the following thesis:

Temperature and Irradiance Dependence of Dye-Sensitized Solar Cell Performance

APPROVED BY
SUPERVISING COMMITTEE:

Halil Berberoglu, Co-Supervisor

Jeremy P. Meyers, Co-Supervisor

Temperature and Irradiance Dependence of Dye-Sensitized Solar Cell Performance

by

Edwin Peng, B.S.

THESIS

Presented to the Faculty of the Graduate School of

The University of Texas at Austin

in Partial Fulfillment

of the Requirements

for the Degree of

MASTER OF SCIENCE IN ENGINEERING

THE UNIVERSITY OF TEXAS AT AUSTIN

December 2010

This is dedicated to my parents, Vincent and Norma Peng, for raising me the right way.

Acknowledgments

I wish to acknowledge my research supervisor, Dr. Halil Berberoglu, for all of his encouragement, guidance, and support throughout my graduate studies.

I wish to acknowledge my co-supervisor, Dr. Jeremy Meyers, for his teachings of electrochemistry and assistance with this thesis.

I acknowledge the assistance of Reeja Jayan and Garrett Salpeter, graduate students of Professor Arumugam Manthiram, for their assistance with the reference solar cell.

I acknowledge the assistance of Professor Rod Ruoff and his group with the scanning electron microscope.

I acknowledge the assistance and friendship of the fellow members of my research group: Altan Ozkan, Kevin Teh, Alexander Ross, Angel Bolhouse, Thomas Murphy, and Onur Taylan.

Last, I acknowledge the support of my family: my wonderful parents, Vincent and Norma, and my sister, Joyce.

Temperature and Irradiance Dependence of Dye-Sensitized Solar Cell Performance

Edwin Peng, M.S.E.
The University of Texas at Austin, 2010

Supervisors: Halil Berberoglu
Jeremy P. Meyers

Dye-sensitized solar cells (DSSCs) are photoelectrochemical cells that offer efficient and potentially economical alternative to conventional solar electricity production technologies. DSSCs belong to the third generation of solar cells and offer several advantages over the solid-state junction solar cells. They utilize materials, such as titanium dioxide that are inexpensive and abundant relative to those used in conventional solar cells. Moreover, DSSCs can be fabricated with simple and scalable manufacturing processes. Finally, in DSSCs, photon absorption and charge-carrier transport are undertaken by different materials, namely molecular dyes and wide band gap semiconductors, respectively. Unlike conventional solar cells, no compromise is necessary between decreasing the band gap for visible light absorption and increasing the band gap to resist photocorrosion. For successful commercialization, a photovoltaic system incorporating DSSCs must operate reliably under a wide range of solar irradiance and operating temperatures.

This experimental study reports the fabrication and characterization of the performance of a DSSC as a function of irradiance and operating temperature. The prototyped DSSCs had (i) nanocrystalline titanium(IV) dioxide, TiO_2, photoanode, (ii) platinum thin film cathode, and (iii) acetonitrile based liquid electrolyte. The photoanodes were sensitized with N-749 dye. The current-voltage characteristics of the DSSCs were measured at operating temperatures from 5 to 50 °C and under 500, 1000, and 1500 W m^{-2} irradiance. The open circuit voltage, V_{OC}, decreased linearly with increasing temperature and had positive, logarithmic relation with irradiance. At temperatures lower than 15 °C and 1500 W m^{-2} irradiance, short circuit current density, J_{SC}, was limited by the diffusion of I_3 in the electrolyte and increased with increasing temperature. At temperatures lower than 15 °C and lower irradiance, J_{SC} increased with increasing temperature due to electron density limited recombination of electrons injected into the TiO_2 conduction band. At higher temperatures, the recombination was dominant over diffusion and J_{SC} decreased with increasing temperature. Moreover, J_{SC} increased linearly with increasing irradiance. The DSSC photoconversion efficiency did not vary appreciably at temperatures lower than 15 °C but decreased with increasing temperature. Finally, the DSSC efficiency increased with increasing irradiance. There was no indication of significant coupling effect of irradiance and temperature on DSSC efficiency.

This study reports for the first time the coupling between irradiance and thermal effects on the operation of DSSCs. The results reported in this

study can be used in recovering kinetic and transport properties that can be used in modeling and optimization of DSSCs.

Table of Contents

List of Figures

Chapter 1

Introduction

The present research addresses the performance characterization of dye-sensitized solar cells (DSSC), a third-generational photovoltaic cell. DSSCs hold the promise to be an inexpensive technology for solar energy conversion in the near future [6, 14].

1.1 Energy Challenges and Solar Energy

The majority of energy consumed in the United States and throughout the world is obtained from fossil fuels: coal, natural gas, and oil [15–17]. These resources are disadvantageous as they are nonrenewable and polluting [3, 15, 17]. Fossil fuels emit carbon dioxide, which current consensus has agreed to be a likely cause of global warming [18–20]. Furthermore, the extraction and processing of coal, natural gas, and oil emit other pollutants, such as lead and mercury, which are harmful to human health [3, 17].

A promising alternative to fossil fuels is solar energy. The sun is a potential source of clean and renewable energy [21]. Using photoelectrochemical cells, solar energy can be directly converted into more useful forms [3, 22]. Nonregenerative photoelectrochemical cells, also known as photoelectrolysis

cells, converts solar energy into chemical fuels such as hydrogen or methane [3, 4]. Regenerative cells, also known as DSSCs, converts sunlight directly into electrical energy [6].

1.2 Dye-Sensitized Solar Cells

DSSCs are unique among the many types of photovoltaic systems such that they mimic photosynthesis [6, 22]. A DSSC uses a dye, like chlorophyll, to absorb light and a thin film semiconductor oxide for charge separation [6, 22]. This grants DSSCs an advantage over conventional, solid-state photovoltaic cells, as there is no need to compromise between increasing band gap to resist semiconductor photocorrosion and decreasing band gap for visible light absorption [22]. DSSCs utilize materials which are inexpensive and abundant, such as titanium dioxide, relative to high materials cost of solid state photovoltaic cells, such as those made from purified silicon [6, 23]. Lastly, DSSCs can be fabricated with relatively simple manufacturing processes, especially continuous roll-to-roll production [6, 23–26]. DSSCs do have the disadvantages of featuring lower solar energy conversion efficiency than solid state cells. Currently, typical silicon photovoltaic panels on rooftops have efficiencies about 15 %. DSSC modules understudy for future commercialization currently have only 8.2 % efficiency [27]. DSSCs also face durability issues with maintaining their liquid or gel electrolytes [6].

1.3 Objectives of the Present Study

The objectives of this study is to characterize the temperature and irradiance dependency of DSSCs. In this study, DSSC with acetonitrile-based electrolyte was chosen due to its widespread use in research and development [28, 29]. The temperature and irradiance ranges were chosen to match the outdoor operation conditions likely to be faced in the continental United States.

1.4 Organization of this Document

Chapter 2 provides the reader with an background in (i) utilization of semiconductors as photoelectrodes in photoelectrochemical cells, (ii) the operating principles of DSSCs, (iii) components of DSSCs with an emphasis on material selection, (iv) characterization of photovoltaic cells, and (v) the factors that affect DSSC's performance. Chapter 3 presents the experimental methods used to evaluate the temperature and irradiance dependence of DSSCs and the results obtained in these studies. Finally Chapter 4 summarizes the conclusions drawn and provides recommendations for future studies. In addition, Appendices A through C provide detailed description of the equipment and instrumentation built and used as a part of this thesis for the performance evaluation of DSSCs. In particular, Appendix A describes quantum efficiency measurement setup, Appendix B describes the polarization curve characterization setup, and Appendix C describes the thin film characterization methods used. The nomenclature used in this document are presented in Appendix D.

Chapter 2

Current State of Knowledge

This chapter presents to the reader an overview of the current state of knowledge of the dye-sensitized solar cells (DSSCs). Section 2.1 provides an brief introduction to the physics of semiconductors as photoanodes in photoelectrochemical cells. In Section 2.2, the operating principles of DSSCs and PECs are introduced. The aspects of material selection for these photoelectrochemical cells are discussed in Section 2.3. An overview of characterization methods used are given in Section 2.4. Finally, Section 2.5 presents the major factors affecting the performance of DSSCs and PECs, with an emphasis on irradiance and temperature.

2.1 Photoelectrodes

Photoelectrodes are made of semiconductor materials [3, 4, 12]. This section summarizes the physics of semiconductors as photoanode materials.

2.1.1 Semiconductors

The electrons of atoms in a semiconductor can only have definite energy levels [21, 30]. The difference in the numerous energy levels of electrons in a

crystal is very small, allowing them to be modeled as energy bands [21, 30]. The valence band is the filled band filled with electrons possessing the highest energy levels [3]. The energy band directly above the valence band is the conduction band [3].

The difference in energy of the conduction band's lowest energy level, E_{CB} and the valence band's highest energy level, E_{VB} is known as the energy band gap, E_g, of that material [3, 30, 31],

$$E_g = E_{CB} - E_{VB}. \tag{2.1}$$

Figure 2.1 summarizes the band gap of conductors, semiconductors, and insulators [1]. An electron in the valence band can move into the conduction band if it receives energy equal to or greater than the band gap [21]. Materials are divided into conductors, semiconductors, and insulators based on the relative position of their conduction and valence bands. [32]. In conductors, there is no band gap; the valence and conduction bands overlap [1]. The presence of electrons at both the valence and conduction bands allows for high electrical conductivity in metals. Insulators have a large band gap, making it difficult for electrons to move to the conduction band and therefore prevent or greatly reduce the conduction of electricity [1]. Semiconductors have a band gap that is in between conductors and insulators [1].

The Fermi energy level is the energy level where the electron has a one half probability of occupation. It is proportional to temperature and can be

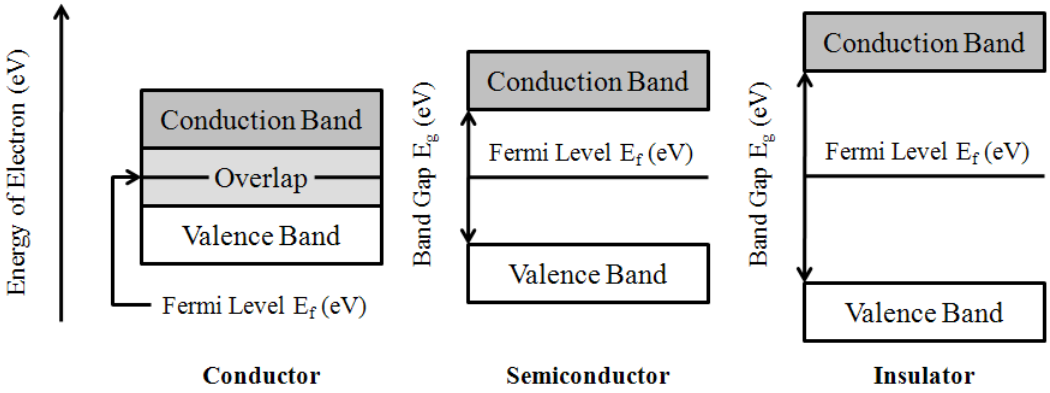

Figure 2.1: Fermi level and band gap of conductors, semiconductors, and insulators [1].

calculated as [3, 21],

$$E_f = \frac{1}{2}\left[E_{VB} + E_{CB} + k_B T \ln\left(\frac{N_{VB}}{N_{CB}}\right)\right], \tag{2.2}$$

where E_f is Fermi energy level, E_{VB} is the highest energy level of the valence band, E_{CB} is the lowest energy level of the conduction band, k_B is the Boltzmann constant, T is temperature, N_{VB} is energy states effective density at the valence band, and N_{CB} is energy states effective density at the conduction band. The locations of Fermi energy level for conductors, semiconductors, and insulators are shown in Figure 2.1. In conductors, the Fermi energy level is located in the overlapping region of the valence and conduction band; it can be used to calculate the velocity of electrically conducting electrons [1]. In semiconductors and insulators, the Fermi level is located in the band gap between conduction and valence bands, as shown in Figure 2.1.

Semiconductors can be "doped" to change their Fermi energy levels and

therefore their electrical properties [3, 21]. Doping replaces a small amount of atoms in a semiconductor crystal with atoms of another element, called an impurity [2, 30]. Small amount of impurity in semiconductors can produce large changes in electrical properties [21]. For example, n-type semiconductors are doped with donor impurities, of concentration N_D, which contributes additional electrons to the semiconductor crystal [21]. These free electrons raises the crystal's Fermi energy level to be slightly below the conduction band as shown in Figure 2.2 [3, 21]. The increased Fermi energy level is defined as [3, 21],

$$E_f = E_{CB} - k_B T \ln\left(\frac{N_{CB}}{N_D}\right). \tag{2.3}$$

Electrons can be easily excited into the conduction band, providing an increase in electrical conductivity.

On the other hand, p-type semiconductors are doped with acceptor impurities, of concentration N_A, which create electron holes. Electron holes are absences of electrons and decrease the Fermi level to near the top of the valence band as shown in Figure 2.2. The decreased Fermi energy level is defined as [3, 21],

$$E_f = E_{VB} + k_B T \ln\left(\frac{N_{VB}}{N_A}\right). \tag{2.4}$$

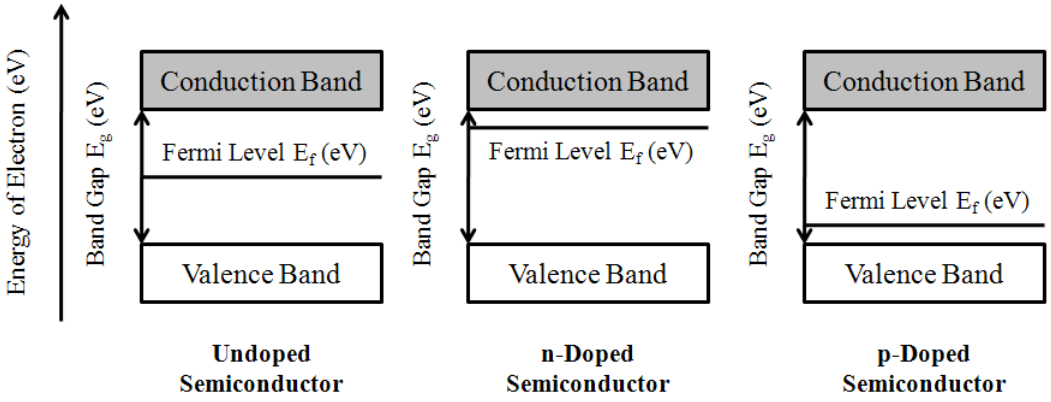

Figure 2.2: Fermi level and band gap for undoped and doped semiconductors [1, 2].

2.1.2 Light Absorption

A semiconductor can absorb photons with energies, E, that are equal to or larger than its band gap, E_g [3, 4, 33],

$$E = h\nu \geq E_g, \tag{2.5}$$

where h is Planck's constant and ν is the photon frequency. The semiconductor converts the photon into electronic charge carriers, namely electrons, e^-, and holes, h^+ [3, 4, 33],

$$h\nu \rightarrow e^- + h^+. \tag{2.6}$$

The absorption and conversion of photons is characterized by the light absorption coefficient, α that is defined depending on the form of charge carrier conversion [3]. If the conversion is due to direct momentum transition, the α is defined as [3],

$$\alpha = A'(h\nu - E_g)^{0.5}, \tag{2.7}$$

where A' is a proportionality constant. For indirect momentum transition, the α is instead defined as [3],

$$\alpha = A'(h\nu - E_g)^2. \tag{2.8}$$

2.1.3 Band Bending

In a photoelectrochemical cell, contact between the semiconductor, as the photoelectrode, with an electrolyte induces bending of semiconductor's energy bands [3, 21, 30]. This occurs at the semiconductor-electrolyte interface due an accumulation of excess charge at a space charge region, an approximately 1 μm thick portion of the semiconductor towards the electrolyte interface [3]. Figure 2.3 (a) shows the band bending of a n-type semiconductor, such as the titanium(IV) oxide (TiO_2) used in this study [3, 4]. Excess electron holes forms an accumulation layer in the space charge region, inducing band bending toward more positive energy level [3]. The semiconductor and electrolyte of Figure 2.3 (a) are shown in equilibrium, so that the semiconductor's fermi level, E_f and the electrolyte's standard redox potential, E_{redox} are equal [3],

$$E_f = E_{redox}. \tag{2.9}$$

Figure 2.3 (b) shows the n-type semiconductor-electrolyte under illumination. The electron-hole pair production generates a photocurrent density, J_{ph}, defined as [3, 21],

$$J_{ph} = e\Phi[1 - (1 + \alpha\ell_{h^+})exp(-\alpha\ell_{SCR})], \tag{2.10}$$

where Φ is incident photon flux, ℓ_{h^+} is hole diffusion length, and ℓ_{SCR} is the length of the space charge region. The electron-hole pairs also decreases the band bending, which induces a photovoltage, V_{ph}, [3, 4, 21],

$$V_{ph} = \frac{k_B T}{e} \ln\left(\frac{J_{ph}}{J_0}\right), \tag{2.11}$$

where J_0 is the saturation current. Finally, V_{ph} is related to the semiconductor fermi level, E_f, and E_{redox} [3],

$$eV_{ph} = E_f - E_{redox}. \tag{2.12}$$

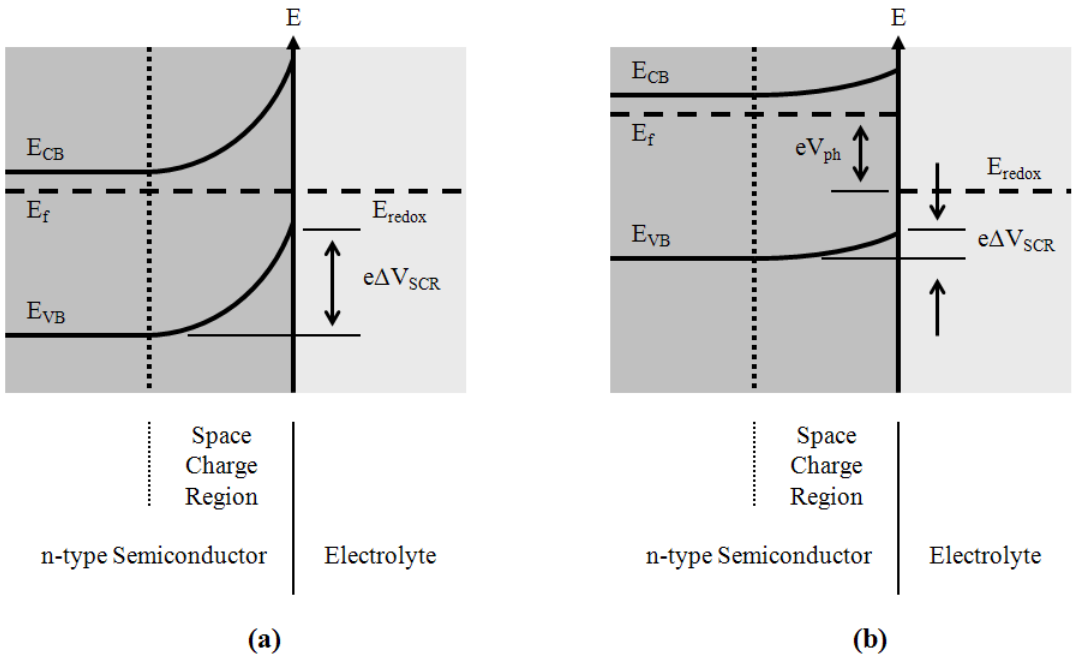

Figure 2.3: Band bending diagram for an n-type semiconductor photoanode at the semiconductor-electrolyte interface under (a) equilibrium dark and (b) light conditions [3, 4].

2.2 Operating Principles of Dye-Sensitized Solar Cells

The distinct feature of DSSC operation is the mimicking of natural photosynthesis [34]. Photon absorption and charge-carrier transport in DSSCs are undertaken by molecular dyes and wide band gap semiconductors, respectively [2, 6, 22, 35]. Figure 2.4 is a DSSC schematic showing its typical components, energy levels, and its seven operating processes. The DSSC shown utilized typical materials: (i) a photoanode made of nanocrystalline anatase titanium(IV) dioxide (TiO_2) thin film sensitized with an adsorbed dye, (ii) an iodide (I^-)/ triiodide (I_3^-) redox couple-based liquid electrolyte, and (iii) a platinum-based (Pt) cathode [3, 6, 22, 36, 37]. The TiO_2 and Pt layers are deposited on an optically transparent conducting oxide (TCO) glass. The seven processes that occur during DSSC operation are divided into four forward, desired processes and three reverse, undesired processes [5, 7, 38]. The time scales associated with these processes are conventionally expressed as the time to complete half the process, known as half-life [5].

2.2.1 Forward Processes

The series of forward processes begin with the absorption of photons by the dye molecules, resulting in an excited state for the dye, Dye* [2, 6, 24, 39],

$$Dye + h\nu \rightarrow Dye^*. \tag{2.13}$$

The dye is limited to absorbing photons having energy equal to or greater than its band gap, E_g, as described by Equation 2.5 [3, 22]. Then, charge separation

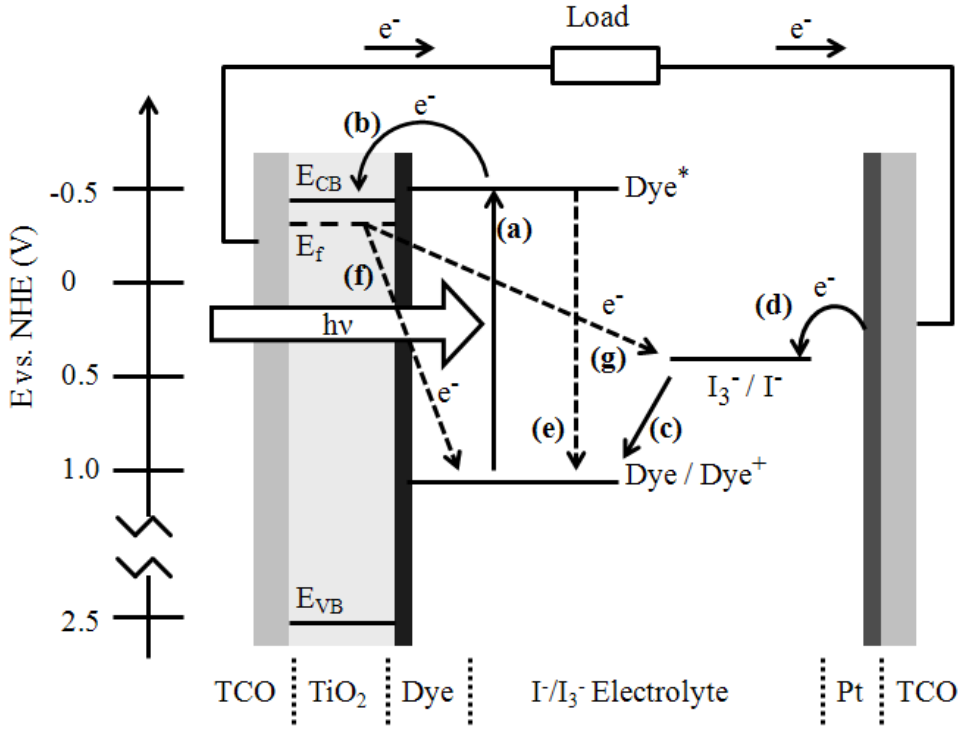

Figure 2.4: Typical DSSC components, energy band levels, and operating processes. The forward processes are (a) photon absorption, (b) electron injection, (c) dye regeneration, and (d) triiodide reduction. The reverse processes are (e) dye relaxation, (f) electron-dye recombination, and (g) electron-triiodide recombination [5–9].

occurs when excited dye molecules inject electrons into the conduction band of the TiO_2 layer, leaving behind the dye molecules in an oxidized state, Dye^+ [2, 6, 24, 39],

$$Dye^* + TiO_2 \rightarrow Dye^+ + e^-(TiO_2). \tag{2.14}$$

Electron injection is a very rapid process with a half-life of approximately 150 ps [5]. For electron injection to occur, the electrical potential of the excited dye must be higher than the conduction band potential of TiO_2, V_{CB} [2, 22].

The transport of the injected electron, $e^-(TiO_2)$, through the TiO_2 is a slower process with a half-life of 100 μs [5]. This electron transport process is predominately diffusive with a diffusion coefficient, $D_{e^-(TiO_2)}$, that is dependent on trapping/detrapping processes [2, 40–42]. The small dimensions of the TiO_2 nanoparticles creates a low net electrical field vector normal to the substate that results in negligible band bending [2, 40]. The small band bending prevents substantial electron transport through migration [2, 30, 40].

The oxidized dye undergos regeneration by the iodide, I^-, present in the electrolyte [2, 6, 24, 39],

$$2Dye^+ + 3I^- \rightarrow Dye + I_3^-. \tag{2.15}$$

This reduction reaction has a half-life of approximately 1 μs, depending on the transport properties of I^- [5].

The injected electrons, $e^-(TiO_2)$, are conducted from the anode to the cathode through an external circuit generating electrical current to deliver power to the external load [6, 42]. Finally, the electron at the cathode, $e^-(Pt)$, reduces the triiodide, I_3^- to regenerate iodide, I^-, [2, 6, 24, 39],

$$I_3^- + 2e^-(Pt) \rightarrow 3I^-. \tag{2.16}$$

This reduction process is limited by I_3^- generation according to the reaction given in Equation (2.15) [2].

2.2.2 Reverse Processes

Reverse processes are undesirable processes which decrease DSSC performance [5, 7, 38]. The three reverse processes in proceeding order are (i) excited dye decay, (ii) electron to triiodide recombination, and (iii) electron to oxidized dye recombination [5, 7, 38]. All reverse processes occur after photon absorption. The first reverse process is relaxation of the excited dye molecules, Dye*, to its original state [5, 7, 38]. The relaxation can be radiative decay through spontaneous emission, essentially the reverse of photon absorption [7, 38],

$$Dye^* \rightarrow Dye + h\nu. \tag{2.17}$$

Alternatively, Dye* can undergo nonradiative relaxation through intermediate states in between the ground and excited states [7, 38]. Instead of photons, energy is released in the form of phonons, or heat. Typically, Dye* are more likely to inject electrons into TiO_2, because dye relaxation occurs at rate approximately 100 times slower, with a half-life of about 12 ns [5, 43].

The electrons injected into the TiO_2 layer, $e^-(TiO_2)$, can recombine with the oxidized dye molecules, Dye^+ [5, 7, 24, 38],

$$Dye^+ + e^-(TiO_2) \rightarrow Dye. \tag{2.18}$$

The half-life for this reaction is approximately 3 μs [5]. Typically, recombination via oxidized dye molecules has an appreciable affect on DSSC performance, as this reaction is in competition with and have similar reaction rates as dye reduction by iodide [5, 38].

Finally, recombination of $e^-(TiO_2)$ can recombine with triiodide, I_3^-, present in the electrolyte [24, 44–46],

$$I_3^- + 2e^-(TiO_2) \rightarrow 3I^-, \tag{2.19}$$

with a half-life of about 1 ms. Recombination with triiodide is the major detrimental process in a DSSC , occurring at the interfaces between TiO_2 and electrolyte or TCO and electrolyte [47, 48]. The mesoporous and nanocrstyalline nature of the TiO_2 film results in large surface areas for such recombination to occur as the surface is not completely covered with adsorbed dye molecules [48].

2.3 Components of Dye-Sensitized Solar Cells

A DSSC contains an anode, a cathode, and electrolyte [6, 24, 37]. The photonanode consists of a wide band gap semiconductor layer sensitized with high absorbance dye deposited on a transparent conductive surface [6, 24, 37]. The cathode is a catalyst layer, also deposited on a transparent conductive substrate [6, 24, 37]. Lastly, the electrolyte facilitate the regeneration of the dye and is sandwiched in between the electrodes [6, 24, 37]

2.3.1 Transparent Conductive Substrate

A transparent conductive substrate (TCS) transmits sunlight and supports the deposition of photoanode and/or cathode layers. Efficient and cost effective DSSCs have multiple requirements for the substrates utilized for deposition of the photoanode and cathode layers [24, 36, 37, 49]. An ideal substrate

must be optically transparent, low electrical resistance, chemically compatible with other DSSC components, structurally stable, light weight, easy to manufacture, and inexpensive [24, 36, 37, 49, 50]. The most commonly used transparent conductive substrate in DSSCs are transparent conductive oxide glass (TCO) and transparent organic conductors [24, 37, 49].

2.3.1.1 Optical Requirements of Transparent Conductors

In DSSCs, the substrate is in between the dye-sensitized semiconductor layer and the incident light. Advanced dyes allow conversion of light with wavelengths in the visible, such as ruthenium "black dye" ($\lambda_g = 920$ nm) can absorb and generate electrons using radiation in the visible and near infrared spectrum [6, 42]. Therefore, the substrate must transmit light in the spectral region where the photoanode is responsive [24, 37, 50]. The spectral transmittance of a substrate can be related to spectral absorptance and spectral reflectance by [50],

$$T_\lambda + A_\lambda + R_\lambda = 1 \tag{2.20}$$

Typically, the spectral transmittance and spectral reflectance are measured using a spectrophotometer [50–54]. Spectral transmittance can be improved by decreasing spectral reflectance [50]. This can be achieved by using anti-reflection treatments specific to the type of transparent conductive substrate [55, 56]. For example, decreasing the iron(III) oxide (Fe_2O_3) content of float glass in TCOs will decrease absorptance and substantially increase transmittance in the near infrared region [50]. Both glass and polymer substrates can

be coated with antireflection (AR) films made from as silica (SiO_2) or magnesium fluoride (MgF_2) nanoparticles [50].

2.3.1.2 Conductivity of Transparent Conductors

Substrates with high conductivity, and conversely low resistivity, are desirable for DSSCs [37]. The bulk resistance of the substrate, R_{TCS}, lowers the voltage produced by the DSSC. The magnitude of this voltage drop, V_{TCS}, is,

$$V_{TCS} = IR_{TCS} \tag{2.21}$$

where I is the DSSC output current. The substrate's conductive layer is modeled as thin film of uniform thickness with electricity conducting only along the substrate's plane. Figure 2.5 shows such a thin film having dimensions of thickness, t, width, w, and length, ℓ and current, I. The resistances of transparent conductive substrates are compared intensively using sheet resistance, R_s, and resistivity, ρ [50]. Sheet resistance is defined as,

$$R_s = R_{TCS}\frac{w}{\ell}. \tag{2.22}$$

It is reported in units of "Ohms per square", $\Omega/\square$, as $R_s = R_{TCS}$ for a square thin film piece. The thin conductive film's resistivity, ρ, the inverse of conductivity, σ, is the product of sheet resistance and conductive film thickness [50, 54],

$$\rho = \frac{1}{\sigma} = R_s t \tag{2.23}$$

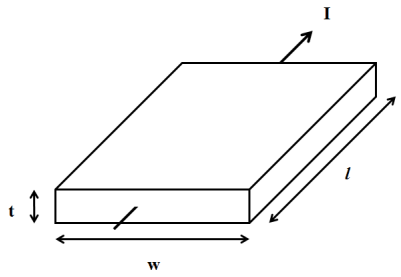

Figure 2.5: Schematic of current flowing through a thin film.

The sheet resistance of a transparent conductive substrate is typically measured using the van der Pauw method with a four-point probe [51–54]. Figure 2.6 shows a schematic of square substrate with four test leads of a four-point probe. The sheet resistance is found using the resistance measured along a vertical edge, R_v, and along a horizontal edge, R_h, according to [10, 11],

$$e^{-\pi R_v/R_s} + e^{-\pi R_h/R_s} = 1. \tag{2.24}$$

The vertical edge resistance is measured by applying a current, I_{12}, from point 1 to 2 and measuring the voltage, V_{34}, across point 3 and 4,

$$R_v = \frac{V_{34}}{I_{12}}. \tag{2.25}$$

The horizonal edge resistance is measured by applying a current, I_{23}, from point 2 to 3 and measuring the voltage, V_{41}, across point 1 and 4,

$$R_h = \frac{V_{41}}{I_{23}}. \tag{2.26}$$

Typical transparent conductors posseses a tradeoff between optical transmittance and sheet resistance [50, 53, 54, 56]. Increasing the thickness will de-

crease sheet resistance, but will result in a decrease in transmittance [50, 53, 57].

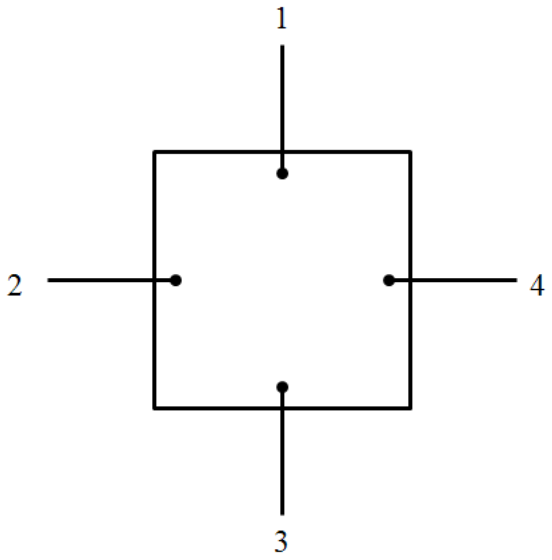

Figure 2.6: Schematic of connections on a sample undergoing conductivity testing by a four-point probe utilizing van der Pauw method [10, 11].

2.3.1.3 Temperature Requirement of Transparent Conductor

The most frequently used semiconductor layer in DSSCs is the mesoporous, nanocrystalline anatase titanium(IV) dioxide (TiO_2) film [6]. During the typical deposition process of the TiO_2 film, the transparent conductive substrate must withstand high temperatures from 450 to 500 °C for 30 minutes [24, 37, 49, 58–60].

2.3.1.4 Examples of Transparent Conductors

Transparent conductive oxide (TCO) glasses are the most commonly researched and currently the most effective substrate for DSSCs [6, 24, 37, 49]. A TCO consist of a conductive layer made of doped wide band gap inorganic oxide semiconductor deposited onto a glass substrate [50–52, 54–56, 61]. The most widely used conductive layers are tin-doped indium(III) oxide (indium tin oxide or ITO), fluorine-doped tin(IV) oxide (FTO), and aluminum zinc oxide (ZnO:Al) [50, 52, 54–56]. Recent research efforts are investigating alternative conductive layer materials, such as tungsten-doped tin(IV) oxide (SnO_2:W) and indium-doped cadmium oxide (CdO:In) [51, 54]. The conductive layer can be deposited onto the glass substrate using sputter deposition, chemical vapor deposition, spray pyrolysis, sol-gel methods, or vacuum evaporation [50, 56]. The optical and electrical properties of a TCO significantly depends on the deposition process [50, 56].

Indium tin oxide (ITO) was the most commonly used conductive layer in DSSCs and other TCO applications [61, 62]. Currently, fluorine-doped tin oxide (FTO) glass substrates are also used in DSSCs [29, 37, 63]. FTO posses the advantages of thermal stability and lower cost with respect to ITO [50, 64]. ITO suffer from conductivity losses attributed to adsorption and desorption of water and oxygen when subject to the high temperatures during deposition of the TiO_2 film [37, 65]. Also, indium prices have increased due to demand for transparent conducting substrates [50]. The TCO is usually the most expensive component of a DSSC [66]. FTO have the potential to be

more advantageous than ITO in DSSCs. FTO do not display high temperature conductivity decrease and have potential to lower costs through simpler manufacturing processes [37].

Graphene Films as Transparent Conductors

The use of thin graphene films (TGFs) as transparent conductors for DSSCs have been the subject of recent research [67]. TGFs are stacks of two dimensional sheets of carbon in honeycomb lattice structure, essentially sheets of two-dimensional graphite [68–70]. Like ITO or FTO films, TGFs are both electrically conductive and transmits large portions of sunlight [57]. They are made from graphite mechanically, through exfoliation, or chemically via oxidation [68]. TGFs can be added on top of existing FTO or ITO film in a transparent conductor [69–71]. With TGFs as the interfacial layer between the inorganic oxide semiconductor film and the TiO_2-dye layer, it improves DSSC performance by suppressing the recombination process described by Equation 2.19 [69–71]. Furthermore, TGFs can replace the inorganic oxide semiconductor film all together [57, 67, 68, 72]. Compared with ITO- and FTO-based transparent conductors, TGFs have the advantages of better adhesion with TiO_2 layers and potentially lower costs due to abundance of graphite [68, 69, 71]. However, TGFs generally have lower optical transmittance in range of photon wavelengths utilized by DSSCs and lower conductivity than ITO or FTO films [57, 68].

Organic Polymers as Transparent Conductors

In the last decade, transparent conductive substrates made from organic polymers have been extensively researched as alternatives to transparent conductive oxide glass [24, 52, 53]. TCOs are disadvantageous for large-scale manufacturing and commercial solar energy of DSSCs because they are inflexible, susceptible to impact damage, high weight, limited in shape, relatively high material cost. [24, 37, 49, 53]. Transparent organic polymer, such as polyethylene terephthalate (PET) and polyimide (Kapton), combined with a conductive oxide semiconductor, address these drawbacks to glass TCOs [24, 37, 49, 52, 53]. By coupling with polymer electrolytes, flexible DSSCs of many differents shapes can be made [37, 49]. More importantly, organic polymers allow DSSCs to be manufactured by large-scale, high speed, and continuous roll-to-roll methods [24, 37, 49, 52, 53]. However, obstacles still remain in utilizing organic polymer substrates. The deposition of the TiO_2 film at the typically required 450 to 500 °C results in the thermal degradation of many transparent polymers [37, 49]. Lowering the deposition temperature to about 150 °C is one method to prevent damage to polymers, but decrease DSSC performance [37, 49]. This is the result of reduced adhesion between TiO_2 film and the substrate due to remaining contaminants and increased portions of rutile phase TiO_2 [37, 49, 73]. The most researched transparent polymer substrate is ITO deposited on PET (ITO-PET) using spin coating or pressing methods [37, 49, 52].

2.3.2 Wide Band Gap Semiconductor Thin Film

The introduction of mesoscopic nanocrystalline anatase TiO_2 films as the wide band gap semiconductor layer greatly improved DSSC performance and made DSSC a feasible alternative to conventional silicon solar cells [6, 22, 37, 45, 74]. These large surface area films allow much higher absorbtion of incident light by the dye due increased optical path length and higher electron diffusion rates [6, 22]. A wide variety of films have been researched, including TiO_2 nanoparticles, nanowires, nanotubes, [6, 60, 75–83]. The DSSC efficiency as well as manufacturability and cost effectiveness are factors in mesoscopic nanocrystalline film design. Lastly, studies show superiority of TiO_2 over alternative wide band gap oxide semiconductors such as tin(IV) oxide (SnO_2) and zinc oxide (ZnO) [6, 84].

2.3.2.1 Sol-Gel TiO_2

Sol-gel is the most common deposition process for TiO_2 layers. TiO_2 nanoparticles are suspended in solvents such as deionized water or ethanol along with a surfactant such as polyvinylpyrrolidone (PVP) [58, 85]. Alternatively, a TiO_2 precursor, such as titanium(IV) *n*-butoxide (TNB) or titanium tetrachloride ($TiCl_4$) is used instead [85, 86]. After applying the titanium containing suspension onto a substrate, evaporation of solvent and surfactant occur [58, 85, 86]. Finally, the TiO_2 undergo sintering to develop the mesoporous nanocrystalline structure [58, 85, 86].

2.3.2.2 Electrospun TiO_2

The electrospinning process produces continuous polymer films composed of interconnecting fibers with diameters on the nm and μm scales [87–90]. TiO_2 can be electrospun into fibrous TiO_2 layers by incorporating a polymer vehicle [81, 83, 91]. A few studies used electrospun TiO_2 to replace some or all of the conventional sol-gel nanocrsytalline TiO_2 layer [23, 82, 92, 93].

2.3.2.3 Incorporation of Carbon Nanotubes

A few studies shown improved DSSC performance when carbon nanotubes (CNTs) are incorporated into TiO_2 layers [94–96]. CNTs are carbon allotropes consisting of single or multiple graphite sheets rolled into a tube. These improvements are attributed to improved injected electron conductivity through the semiconductor layer. There exist an optimum concentration of CNTs in the semiconductor layer, since its a tradeoff between improved conductivity at higher concentration and increased photon absorption at lower CNT concentration [94–96].

2.3.3 Sensitizing Dye

The dye in DSSCs must have a wide absorption band and electron generation rate in the solar spectrum and adhere well to the nanocrystalline semiconductor film for efficient charge transfer [6]. Dye molecules require carboxyl (-COOH), carbonyl (-CO), or hydroxyl (-OH) functional groups for effective adsorption onto [97–99].

2.3.3.1 Ruthenium-Based Dyes

Ruthenium based dyes are currently the most effective DSSC sensitizing dyes [6]. Chemical structure of ruthenium dyes are typical ruthenium complexes with carboxyl (-COOH) functional groups at the ends of the ligands [6]. Ruthenium dyes form an adsorbed monolayer over the TiO_2 film, decreasing exposure of TiO_2 with liquid electrolytes and therefore prevent recombination via triiodide (Equation 2.19). The primary drawbacks to ruthenium dyes are the price of ruthenium and potential environment hazards presented by this heavy metal [66]. Ruthenium dyes are usually the most expensive component of a DSSC after the TCOs [66].

Adsorption of dyes is performed by submerging the wide band gap semiconductor layer in a dye solution. Typically, organic solvents are used for adsorption of ruthenium-based dyes, as ruthenium-based dyes cannot adsorb in aqueous solutions [74].

2.3.3.2 Natural Dyes

Dyes occurring naturally in plant material are a attractive options. Such natural dyes are readily available and environmentally friendly [97, 98, 100]. Unfortunately, DSSCs with natural dyes possess inferior efficiency and short operating lifetime [99, 100]. Carotenoids and chlorophyll a, b, and d dyes, for instance, are ineffective TiO_2 sensitizers due to presence of alkyl (CH_3) functional groups and long alkane chain [98, 101]. Both chemical structures hinder proper adsorption [97, 98]. Presently, the most promising natural dyes

are those with anthocyanin structure [39, 98, 99, 102]. Anthocyanin-based dyes adsorb well with TiO_2 by chelation through the presence of carbonyl (-CO) and hydroxyl (-OH) functional groups [98, 101]. DSSCs with efficiencies up to 1.5% using these natural dyes has been reported [39].

2.3.3.3 Mordant Dyes

Millington *et al.* introduced the use of mordant dyes in DSSCs [66]. Mordant dyes are a numerous group of low-cost dyes used in the textile industry [66]. The most effective dye was mordant black 5 [66]. Mordant dyes are also found to be comparable with ruthenium N3 dye in 15-hour longevity studies [66].

2.3.4 Electrolyte

2.3.4.1 Solvents and Ion Sources

The most effective DSSC electrolytes are liquid-based and utilize the iodide/triiodide redox couple [6, 29, 103]. Such electrolytes must contain a source of iodide, iodine, and solvent [29]. Iodide is present in the electrolyte by dissociation of an ionic compound containing iodine, such as lithium iodide (LiI) [29, 84]. Triiodide is formed by the following reaction [104, 105],

$$I_2 + I^- \rightarrow I_3^-. \tag{2.27}$$

This reaction could be assumed to be complete so that each all iodine (I_2) are consumed [104, 105]. The solvents are typically organic, usually acetonitrile, and nonaqueous so that ruthenium-based dyes will not desorb from semicon-

ductor layer [84, 97, 106]. Iodide and triiodide ions have high diffusion coefficients in acetonitrile solutions [28]. Aqueous solutions are usually not used, as ruthenium-based dyes desorb in the presence of water [74]

Alternatively, liquid electrolytes can utilize ionic liquids containing iodide anions [29, 107]. Ionic liquids (ILs) are liquids at room temperature and act as both the solvent and iodide source [29, 108]. The most widely research ionic liquids for DSSCs are 1-propyl-3-methyl-imidazolium iodide (PMII), 1-ethyl-3-methyl-imidazolium dicyanamide (EMI-DCA), and 1-butyl-3-methyl-imidazolium tetrafluoroborate (BMI-TFB) [29, 108]. DSSCs utilizing ILs electrolytes last longer, but at the expense of decreased efficiency due to lower ionic diffusion [29, 107, 109].

2.3.5 Cathode

Typical DSSC cathodes consists of a platinum (Pt) catalyst layer deposited on a transparent conductive substrate [6, 110–112]. Current research entails finding alternatives to replace the expensive platinum [111, 113–115]. Alternatives include stainless steel sheet metal, and single-walled carbon nanotubes [113–115].

2.4 Performance of Photoelectrochemical Cells

The most pertinent measure of photoelectrochemical cell is the solar energy conversion efficiency, usually referred to as the photoconversion efficiency, and is defined for DSSCs and PECs in Section 2.4.1. To better understand the

factors determining photoconversion efficiency and to search for methods of improving it, diagnostic experiments monitoring the charge separation, transport and collection are performed.

2.4.1 Solar Energy Conversion Efficiency

The polarization curve, i.e. the current-voltage (IV) curve, displays the simultaneous variation of a photovoltaic cell's voltage and current at load resistances varying from zero (short circuit) to infinity (open circuit) [12]. It is a very important characteristic of any photovoltaic cell [12]. The current of a photovoltaic cell is proportional to its area [12]. Therefore, the current density, J, ratio of current to cell area, is used in place of current in IV curves. The cell's electrical power output per area, power density, P, is calculated at each current density-voltage combination,

$$P = VJ. \tag{2.28}$$

Figure 2.7 shows a set of IV and PV curves for a DSSC. As the current goes to zero, the cell voltage approaches open circuit voltage, V_{OC} and as the voltage goes to zero cell current approaches the short circuit current density, J_{SC} [12]. The theoretical power output density is the product of open circuit voltage and the short circuit current density [12]. The actual maximum power density, P_{max}, with its corresponding current density, J_{max} and V_{max} occurs at a specific resistance in between short circuit and open circuit conditions. The ratio of

maximum to theoretical power density is the fill factor, FF, [12, 20],

$$FF = \frac{P_{max}}{J_{SC}V_{OC}} \tag{2.29}$$

The overall photoconversion efficiency, η, rates the photovoltaic cell's ability to convert light into electricity. It is the ratio of the cell's maximum output power density to the power density of incident light, irradiance, G, [6, 12, 20],

$$\eta = \frac{P_{max}}{G}. \tag{2.30}$$

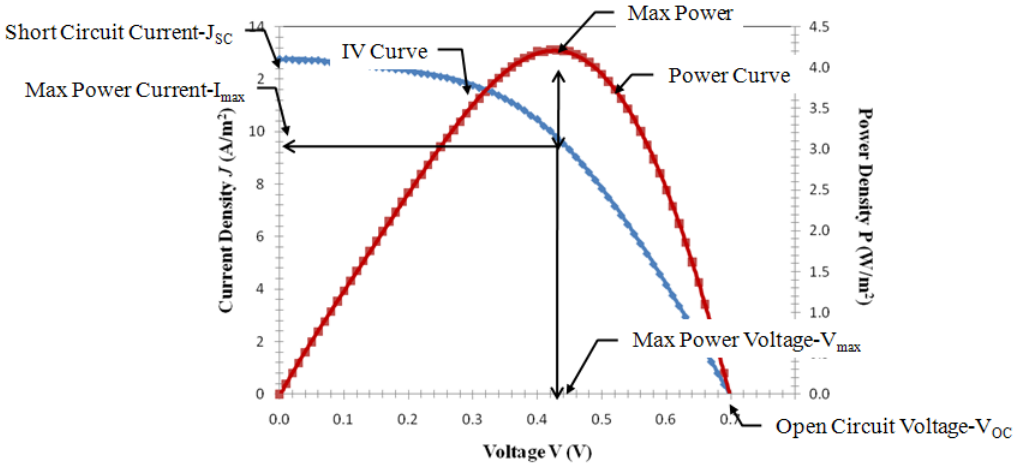

Figure 2.7: Sample current-voltage (blue) and power-voltage (red) curves for a photovoltaic cell [3, 12].

2.4.2 Quantum Efficiency

Quantum efficiency, η_Q, is the measure of a photoelectrochemical cell's ability to convert photons into electron-hole pairs. There is two types of quantum efficiency, external, η_{EQ}, and internal, η_{IQ}.

2.4.2.1 External Quantum Efficiency

External quantum efficiency, η_{eq}, also known as incident photon to current conversion efficiency, IPCE, is the ratio of converted photons to the total photons incident on the cell [3, 4],

$$\eta_{EQ} = \frac{\text{converted photons}}{\text{incident photons}} = \frac{hc}{e}\frac{I_{ph,\lambda}}{G_\lambda \lambda}, \tag{2.31}$$

where h is Planck's constant, c is speed of light in vacuum, $I_{ph,\lambda}$ is the cell's spectral photocurrent, and G_λ is spectral incident irradiance.

2.4.2.2 Internal Quantum Efficiency

Internal quantum efficiency, η_{iq}, or absorbed photon to current conversion efficiency, APCE, is the ratio of converted photons to total photons absorbed by the photoanode [3, 4],

$$\eta_{IQ} = \frac{\text{converted photons}}{\text{absorped photons}} = \frac{hc}{e}\frac{I_p(\lambda)}{G_{a,\lambda}\lambda}, \tag{2.32}$$

where $G_{a,\lambda}$ is absorbed spectral incident irradiance by the photoanode. Photons absorbed by the photoanode is less than total incident photons as a portion of incident photons are reflected and transmitted. Ideally, internal quantum efficiency is a better evaluation of the properties of the photoanode, as it is independent of other cell components.

2.5 Factors Affecting Performance of Dye-Sensitized Solar Cells

Irradiance and temperature are the two factors on DSSC performance examined by this study.

2.5.1 Temperature

Previous studies on liquid-electrolyte DSSCs demonstrated two processes that are affected by temperature [9, 29, 109, 116]. The first process is triiodide, I_3^-, diffusion in the electrolyte that sets a maximum current the DSSC may generate at a given temperature [9, 29, 109, 116]. A positive relationship between diffusion and temperature exists such that triiodide diffusion and hence the maximum DSSC current increases with increasing temperature [9, 29, 109, 116]. The second process is the recombination of injected electrons in the photoanode, as described by Equation 2.18 and 2.19 [9, 29, 109, 116]. Recombination processes decrease the DSSC current and their rate increases with increasing temperature.

Diffusion

The reduction of oxidized dye molecule at the photoanode and triiodide at the cathode are dependent on charge transfer by the diffusion of iodide, I^-, and triiodide, I_3^-, ions in the electrolyte. It is the diffusion of I_3^- that limits DSSC current as its diffusion coefficient, $D_{I_3^-}$, is much lower than that of I^- in all common DSSC electrolyte solvents [28, 104, 117]. The triiodide diffusion

coefficient, $D_{I_3^-}$, has exponential dependence on temperature according to the Arrhenius equation [9],

$$D_{I_3^-} = D_0 e^{\left(\frac{-Q}{RT}\right)}, \tag{2.33}$$

where D_0 is the maximum triiodide diffusion coefficient and Q is activation energy per mole. [9]. For PMII based electrolytes, approximate values for D_0 and Q are 1.3 $\times 10^{-11}$ m^2 s^{-1} and 1.8 J mol^{-1}, respectively. The maximum DSSC current density, $J_{SC,max}$, is proportional to the triiodide diffusion coefficient [9, 104],

$$J_{SC,max} = \frac{2 z_{e^-} e D_{I_3^-} c_{I_3^-} L}{d_e}, \tag{2.34}$$

where z_{e^-} is the number of electrons transferred, e is the elementary charge, $D_{I_3^-}$ is the diffusion coefficient of I_3^-, $c_{I_3^-}$ is the concentration of I_3^- in the electrolyte, L is the Avogadro constant, and d_e is the distance between the electrodes. The short circuit current density, J_{SC}, of the DSSC cannot exceed $J_{SC,max}$ [8, 9]. When the DSSC current is limited by I_3^- diffusion, the temperature dependency of I_3^- diffusion is dominant and J_{SC} increases with temperature [9, 29, 109]. Increased DSSC current densities corresponds with increased DSSC efficiency, thus, improved DSSC performance is expected at higher DSSC temperatures [9, 29].

Recombination

The rate of DSSC electron recombination processes is also temperature dependent [9, 29, 109, 116]. The recombination of injected electrons in the TiO_2 film with triiodide in the electrolyte have been recognized as the dominant

recombination process in DSSCs [8, 46–48]. As described in Equation 2.16, this reverse process occurs at the interface between the mesopours TiO_2 film and the electrolyte when some injected electrons in the TiO_2 conduction band reduces I_3^- [24, 44–46]. The recombination produces a recombination current density, J_r, that is proportional its recombination reaction rate, k_r, [8],

$$J_r = ek_r c_{I_3^-}(n - n_0), \tag{2.35}$$

where n and n_0 are electron concentration in the TiO_2 layer under illumination and dark conditions, respectively.

Literature presented two different approaches to determining k_r. The first method uses the assumption that recombination in DSSCs is a heterogeneous electron transfer and is therefore limited by the electric potential [118]. The k_r is therefore exponential dependence on temperature according to the Arrhenius equation, just like the triiodide diffusion coefficient, [30, 118],

$$k_r = k_0 \, exp\left(\frac{-\beta\eta e}{k_B T}\right), \tag{2.36}$$

where k_0 is the standard reaction rate constant, β is a transfer coefficient related to the activation energy for recombination reaction, η is the overpotential, and k_B is the Boltzmann constant.

The second approach assumes that recombination is limited by electron transport in the TiO_2 film. Therefore, k_r is dependent on electron density, n [41, 119–121]. Electron density, in turn, is a function of position in the TiO_2 photoanode and time [119, 121]. The basic method to model n and

the resulting k_r is to assume one dimensional diffusion transport for electrons within the TiO_2 film, where x is 0 at the TCO-TiO_2 interface and is d_t at the TiO_2-electrolyte interface [41, 119, 122, 123]. Then, the k_r given location x, $k_r'(x)$, is defined as,

$$k_r'(x) = k_0' \left(\frac{n}{n_0} \right)^{\frac{T_c - T}{T_c}}, \tag{2.37}$$

where n is total electron density, n_0 is electron density in the dark, and T_c is a characteristic temperature approximately 1000 K [41, 119]. The overall k_r would be the integral of $k_r'(x)$ across the thickness of the TiO_2 film. The relation of $k_r'(x)$ described in Equation 2.37 indicates that the recombination rates decreases with increasing temperature.

The recombination current density decreases the photocurrent density, J_{ph} [8, 9, 29, 44, 45],

$$J_{ph} = J_{inj} - J_r, \tag{2.38}$$

where J_{inj} is the electron injection current. The J_{inj} results from photon absorption and electron injection processes described by Equation 2.13 and 2.14 in Section 2.2 and is expressed as,

$$J_{inj} = e\mathcal{A}\Phi, \tag{2.39}$$

where $\mathcal{A}$ is optical absorptance and Φ is incident photon flux.

The DSSC short circuit current density, J_{SC}, is [8],

$$J_{SC} = J_{ph} - J_d = J_{inj} - J_r + J_d, \tag{2.40}$$

where J_d is the dark current density. In DSSCs, J_d is typically much smaller than the recombination current density, hence, the J_{ph} can be taken as the J_{SC} [8],

$$J_{SC} = J_{inj} - J_r. \tag{2.41}$$

Assuming constant irradiance and therefore constant J_{inj}, J_{sc} decreases with increasing recombination of the injected electrons and thus with increasing temperature. When this recombination process is dominant, DSSC performance decreases with temperature [9, 29].

In addition to affecting DSSC current, the increased injected electron to triiodide recombination rate also decreases the maximum DSSC voltage, the open circuit voltage, V_{OC}, [8, 9, 44–46],

$$V_{OC} = |V_{FB} - V_{redox}| = \left[\frac{k_B T}{e}\right] \ln\left[\frac{\Phi_{inj}}{c_{e^-(TiO_2)} k_{r2)}}\right], \tag{2.42}$$

where V_{FB} is the TiO_2 flat band potential, V_{redox} is the potential of reduction-oxidation reaction in the electrolyte, Φ_{inj} is the charge injection flux into TiO_2 conduction band, and $c_{e^-(TiO_2)}$ is the concentration of injected electrons at TiO_2 surface. The recombination reaction rate is the dominant temperature dependence parameter in Equation (2.42) so that DSSC open circuit current decreases linearly with increase in temperature [9, 124]. At open circuit, electron density is high in the photoanode so that the rate k_r is proportional to the magnitude of the slope of the open circuit voltage versus temperature plot [9, 124]. Thus, increasing temperature can be detrimental to DSSC performance by decreasing both photocurrent and photovoltage through increased

recombination [8, 9, 29].

Nitrogen Heterocyclic Compounds

Lastly, the presence of nitrogen heterocyclic compounds, NHCs, in the electrolyte may also alter the DSSC's temperature dependence. NHCs can coadsorb onto the TiO_2 thin film and fill up space not taken up by the dye, decreasing the available sites for recombination via Equation 2.19 [46]. Lower recombination rates will result in higher output voltage and current throughout all temperature and I_2 concentrations [9, 29]. Temperature also interacts with NHCs directly through ionic crystal formation. NHCs such as imidazoles (MBI) can form the $(MBI)_6(I^-)(I_3^-)$ crystal following in the electrolyte [125]. Crystal formation will decrease available I_3^- concentration in the electrolyte, decreasing both output DSSC current (Equation 2.34 and recombination (Equation 2.19). The crystal formation decreases with increasing temperature [46].

Previous Work

The most comprehensive temperature study to date was performed by Berginc *et al.* [9, 29]. Performance was evaluated under one level of irradiance, 1000 W/m^2, and temperature from 5 to 55 °C for three types of DSSCs with different ionic liquid based electrolytes. The concentration of triiodide was also varied by altering the concentration of iodine, I_2, in all three electrolytes. Furthermore, the authors also reported on the performance of a fourth type

of DSSC with an electrolyte containing 0.05 M I_2, 0.1 M LiI, 0.6 M PMII, and 0.1 M lithium iodide (LiI) in acetonitrile solution. The authors concluded that DSSC performance for all four electrolyte types was strongly dependent on both temperature and the iodine, I_2, concentration [9, 29]. The tradeoff between the temperature dependencies of triiodide diffusion and electron recombination was confirmed in the relations of J_{SC} versus temperature [9, 29]. For all electrolytes, the V_{OC} decreased linearly with increasing temperature, with the slope $\mathrm{d}V_{OC}/\mathrm{d}T$ increasing in magnitude with increasing I_2 concentration. For the acetonitrile-based electrolyte, the injected electron to triiodide recombination was found to be dominant over the majority of the temperature range [29]. The decreasing DSSC efficiency with temperature mirrors the decrease in V_{OC} with increasing temperature [29]. Thus, V_{OC} was more influential than J_{SC} in determining the temperature dependence of DSSC performance [29].

2.5.2 Irradiance

The relationship between intensity of sunlight and the DSSC performance has been investigated in literature and is relatively well understood. The photon flux incident on the DSSC, Φ, is directly proportional to irradiance, G [3, 8, 126],

$$\Phi = \int_{\lambda_{min}}^{\lambda_{max}} \frac{G_\lambda \lambda}{hc}\, d\lambda, \tag{2.43}$$

where G_λ is spectral irradiance, h is Planck's constant and c is speed of light in vacuum. The irradiance, G, is the integration of the particular light source's

G_λ from the minimum, λ_{min} to maximum wavelength, λ_{max} [3, 126],

$$G = \int_{\lambda_{min}}^{\lambda_{max}} G_\lambda \lambda \, d\lambda. \tag{2.44}$$

If the light source's irradiance level does not impact its spectral output, then Φ has a linear relationship with G [3, 8, 126].

Equations 2.39 and 2.41 indicates that with negligible or a G dependent recombination current, the DSSC current has linear relationship of DSSC short circuit current density, J_{SC}, with irradiance. Several experimental results have shown this phenomena [8, 127].

This linear relationship would not hold true under two conditions. First, the diffusion limitation on maximum DSSC current described in Section 2.5.1 will occur at higher irradiances with larger magnitude of J_{inj} and thus resulting J_{SC} [9]. In DSSCs where the I_3^- concentration is low, the J_{SC} to G relationship deviates negatively from linearity due to low I_3^- concentration at the cathode [8].

The relationship of DSSC voltage with Φ is logarithmic, as seen in Equation 2.42. Therefore, open circuit voltage, V_{OC}, should demonstrate a positive logarithmic dependence with irradiance [8, 118, 128].

Chapter 3

Fabrication and Characterization of Liquid Electrolyte Dye Sensitized Solar Cell

The chapter describes the fabrication and characterization of a DSSC having an acetonitrile based electrolyte. To the best of the authors knowledge, it reports for the first time the coupled effects of irradiance and temperature on the operation and performance of the DSSCs

3.1 Design And Fabrication Of The Dye-Sensitized Solar Cells

3.1.1 Nanocrystalline TiO_2 Layer Deposition and Sintering

Each DSSC utilized a mesoporous, nanocrystaline TiO_2 layer made from a TiO_2 nanoparticle colloidal suspension (sol-gel) prepared using state of the art methods [45]. 6 g of TiO_2 nanopowder (Degussa, P25, Germany) was mixed with 0.1 mL acetylacetone (Fluka, 10916, Germany) and 4.5 mL deionized water (Thermo Scientific, D4641, MA, USA). The deionized water was added in 0.5 mL intervals and the suspension was ground in a mortar and pestle until it was visibly uniform after each addition of deionized water.

The transparent conductive substrate used was a fluorine-doped tin oxide (FTO) glass plate (Hartford, TEC-8, IN, USA) measuring 25×25×3.2

mm with the sheet resistance of 6-9 Ω/sq. A film having a circular area of 0.33 cm^2 was deposited using the doctor-blade method. The solvents were evaporated from the film in room temperature under atmospheric conditions. Then, the TiO_2 film was sintered in a burnout oven (Vulcan, 3-550, KY, USA) at 450 °C for 30 min starting at room temperature at a rate of 40 °C/min. Lastly, the TiO_2 film was cooled to 70 °C slowly over 90 minutes to prevent glass cracking.

A scanning electron microscope (SEM) (FEI, F600, OR, USA) was used to physically characterized the finished nanocrystalline TiO_2 films. Figure 3.1 shows the SEM image of the nanocrystalline TiO_2 film. The interconnected TiO_2 particles have diameters ranging from 15 to 55 nm, with an average diameter of 28 nm. The thickness of the TiO_2 film was determined to be 6.6 ± 0.6 μm using a profilometer (Dektak, 6M, NY, USA).

3.1.2 Dye-Sensitization of TiO_2

The nanocrystaline TiO_2 layer was sensitized with ruthenium N-749 dye (triisothiocyanato-(2,2':6',6-terpyridyl-4,4',4-tricarboxylato)ruthenium(II) tris(tetra-butylammonium)), commonly known as "black dye", (Solaronix, 620-1H3TBA, Switzerland) [6]. First, black dye was dissolved in 200 proof ethanol (Decon Labs, ACS limits, PA, USA) at a concentration of 20% w/v. The black dye solution was magnetically stirred (Fisher Scientific, Isotemp, PA, USA) at 400 rpm for 5 hours at room temperature and under atmospheric pressure. Then, the TiO_2 film at 70 °C was submerged in the dye solution for 24 hours at room

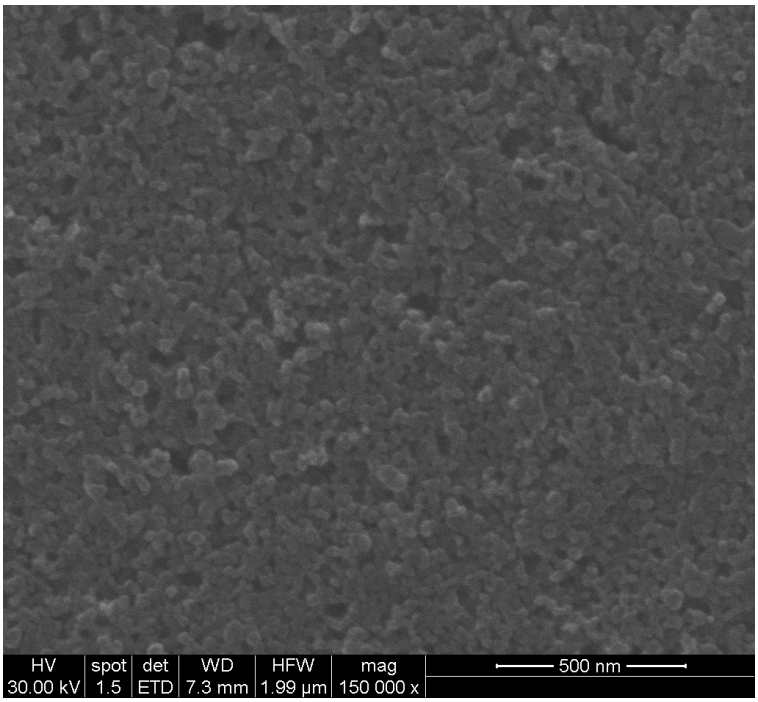

Figure 3.1: SEM image of the nanocrystalline structure of the sintered TiO_2 film.

temperature and under atmospheric pressure [9, 74]. Finally, the photoanode was removed from the dye solution and rinsed in 200 proof ethanol (Decon Labs, ACS limits, PA, USA) [74].

3.1.3 Electrolyte Preparation

The electrolyte used in the experiments was acetonitrile-based and prepared by adding (i) 0.2 M of anhydrous lithium iodide (LiI) (Fisher Scientific, AC20359, PA, USA), (ii) 0.6 M of 1-methyl-3-propylimidazolium iodide (PMII) (Alfa Aesar, H27682, MA, USA), (iii) 0.06 M of anhydrous iodine (I_2) (Sigma-Aldrich, 207772, MO, USA), and (iv) 0.5 M of the nitrogen heterocyclic

compound 1-methylbenzimidazole (MBI) (Alfa Aesar, B25472, MA, USA) to acetonitirile (Sigma-Aldrich, 241004, MO, USA) [28]. The electrolyte solution was magnetically stirred at 1200 rpm for 24 hours at room temperature and under atmospheric pressure.

3.1.4 Platinum Layer Deposition and Sintering

A transparent platinum film cathode with 0.64 cm^2 area was fabricated by depositing a platinum precursor (Solaronix, Platisol, Switzerland) on FTO glass plate using the doctor-blade method [74]. The solvents were evaporated at room temperature for 10 min. Then, the film was sintered in the burnout oven (Vulcan, 3-550, KY, USA) at 400 °C for 30 min starting at room temperature and increasing at a rate of 40 °C/min [74]. Finally, the cathode was rinsed in 200 proof ethanol (Decon Labs, ACS limits, PA, USA) [74].

3.1.5 Cell Assembly

Figure 3.2 shows the schematic of (a) the top and (b) side view of the assembled DSSC. The cell was sealed using one layer of 60 μm thick Surlyn film (Solaronix, SX1170-60, Switzerland). The electrolyte was injected into the cell through pre-drilled holes on the FTO glass plate with the dye-sensitized TiO_2 photoanode layer. The holes were sealed by another layer of Surlyn film with a glass cover slip. Electrical contacts were made by depositing via doctor-blade silver conductive epoxy (MG Chemicals, 8331-14G, Canada) films on the photoanode and cathode lips. Lastly, the assembled DSSC, shown in Figure

3.3 was placed in the dark under open voltage condition for 12 hours to allow full penetration of the electrolyte into the photoanode layer [9].

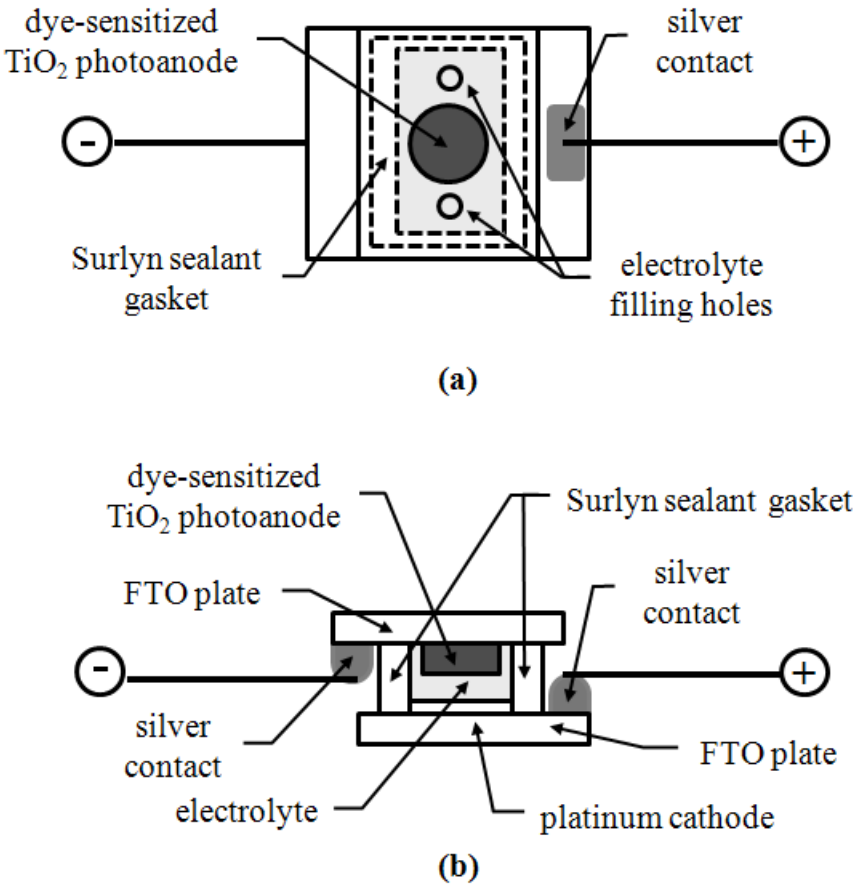

Figure 3.2: Schematic view of the (a) top and (b) side of fabricated DSSCs.

3.2 Polarization Curve Measurement

Figure 3.4 shows the schematic of the system used for measuring the DSSC polarization curves. An AM 1.5 Global filter (Newport, 81094, CA, USA) was used in conjunction with the 300 W Xenon lamp (Newport, 66984,

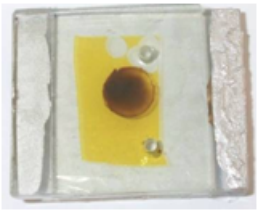

Figure 3.3: Photograph of the top view of a fabricated DSSC.

CA, USA) to simulate sunlight. The polarization curve measurement setup was compared with a reference monocrystalline silicon photovoltaic cell certified by the National Renewable Energy Laboratory (Hamamatsu, S1133A KG5 Filtered, Japan). Figure 3.5 compared the polarization curve of this reference cell obtained with our setup with polarization curve provided by NREL. The measurements agreed with each other within 0.10% for J_{SC}, 4.4% for V_{OC}, and within 3.0 % for η.

The DSSC performance was measured at three irradiances, G, namely 500, 1000, and 1500 W m^{-2} measured with a calibrated photodiode. A source meter (Keithley, 2400, OH, USA), supplied the DC voltages from 0 to 0.75 V at 25 mV intervals and measured the corresponding DSSC currents. A 1 s delay occurred between supplying the voltage and measuring the current. The η, J_{SC}, and V_{OC} were calculated from the polarization data.

3.3 Temperature Control

The temperature of the DSSC was varied from 5 to 50 °C in 5 °C intervals. The temperature was measured using three thermocouples attached

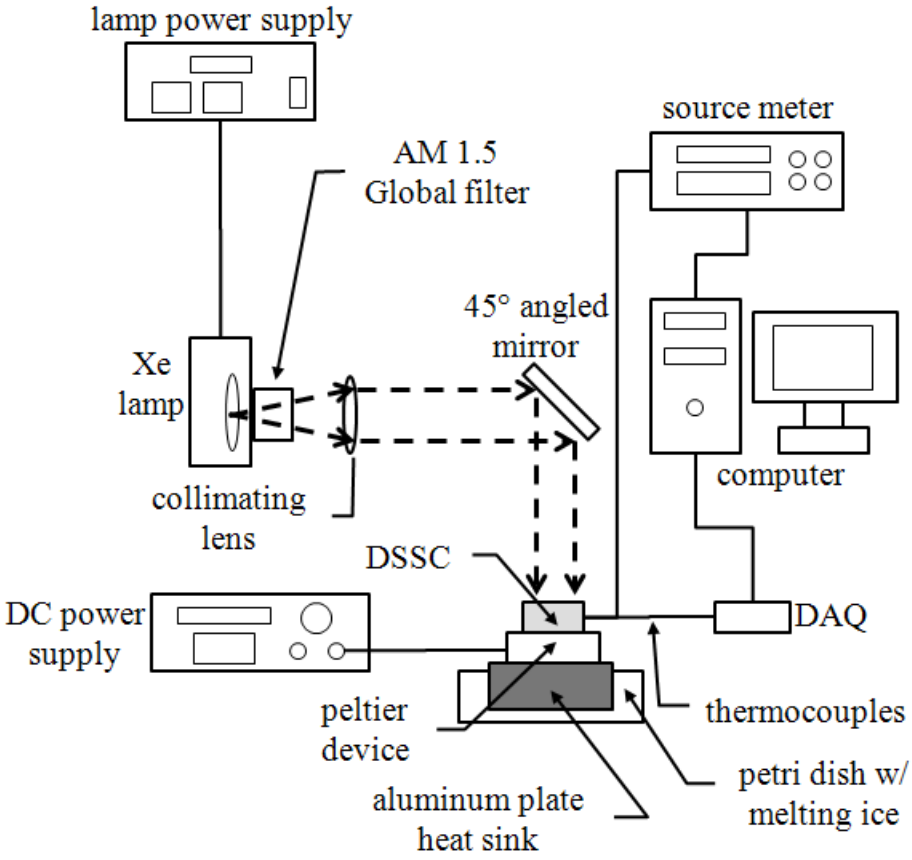

Figure 3.4: Schematic of the temperature controlled photovoltaic cell polarization curve measurement system.

either sides of the cell using heat resistant tape (Fisher Scientific, 19-160-0098, USA). A Peltier device (Marlow, RC12-8-01, TX, USA), measuring an area of 40×40 mm with a thickness of 3.6 mm, powered by a programmable DC power supply (Agilent, E3642A, CA, USA) was used to control the DSSC temperature. At temperatures below room temperature, the DSSC and Peltier device was placed on a heat sink consisting of a small aluminum plate submerged in melting ice. A data acquisition device (Personal DAQ54, iOtech, OH, USA)

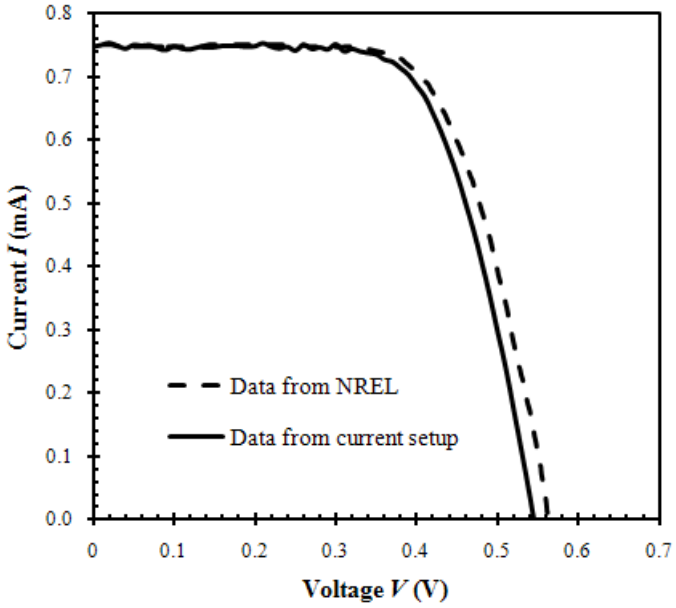

Figure 3.5: Comparison of IV curve obtained using the polarization curve measurement setup with NREL calibration data.

recorded the thermocouple readings throughout the experiments. If the temperature readings on both sides of the cell is within 1 °C, the temperature is assumed constant throughout the cell and is determined by the mathematical mean of all thermocouple readings.

3.4 Results and Discussion

Figure 3.6 shows the short circuit density, J_{SC}, and the open circuit voltage V_{OC}, as a function of temperature from 5 to 50 °C at three irradiances, G, namely 500, 1000, and 1500 W m^{-2}. Figure 3.6(a) identifies two thermal regimes, where at temperatures lower than 15 °C the J_{SC} increases

with increasing temperature and where temperatures larger than 15 °C J_{SC} decreases with increasing temperature. This J_{SC} behavior was attributed to the limitation of J_{SC} by recombination of electrons with triiodide, I_3^-, in the electrolyte. At lower temperatures, the recombination process is limited by electron density in the photoanode. The recombination will decrease with increasing temperature via the recombination rate determined by 2.37. However, at the high temperature thermal region, the J_{SC} was constrained by the electron transfer-limited recombination. The injected electrons in the TiO_2 conduction band recombined with I_3^- in the electrolyte at a rate that increased with increased temperature, as determined by Equation 2.36. Since recombination current density, J_r, is linearly proportional to the recombination rate, the photocurrent density, J_{ph}, and J_{SC} decreases with increasing J_r. These two thermal regions of J_{SC} was similar to previous temperature dependency studies of DSSCs [9, 29, 109, 116, 129]. It is possible that the J_{SC} was limited by diffusion of triiodide ions in the electrolyte below 15 °C at the high irradiance of 1500 W m^{-2}. As seen in Equation 2.33 and 2.34, the limiting current, J_{lim}, increased with increasing temperature, and thus J_{SC} increased with increasing temperature.

On the other hand, figure 3.6(b) indicates that open circuit voltage, V_{OC}, was found to be linearly dependent on temperature at all three irradiances. This linear dependence was the result of the previously mentioned relation between injection electron recombination and V_{OC}, described in Equation 2.42. The linear dependency hads been characterized many times in previous

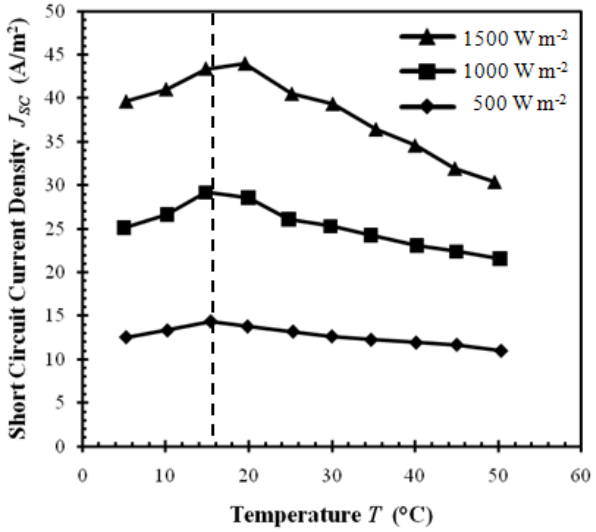

Figure 3.6: (a) Short circuit current density and (b) open circuit voltage, as functions of temperature from 5 to 50 °C at three irradiances 500, 1000, and 1500 W m^{-2}.

DSSC research [9, 29, 109, 116, 124, 128, 129]. The magnitude of $V_{OC}/\mathrm{d}T$ versus temperature is positively dependent on recombination probability of the DSSC, with solid-state DSSCs possessing steeper slopes than liquid electrolyte DSSCs [124].

Figure 3.7(a) shows J_{SC} at 25 °C as a function of irradiance. The coupled effect of irradiance with temperature dependency was that J_{SC} was found to generally have a linear relation with irradiance, G, over the 5 to 50 °C. In the diffusion dominated thermal region, this is likely due to the increase in concentration of I_3^- in the electrolyte, $c_{I_3^-}$. The increase in oxidized dye molecules was due to increased irradiance via the absorption of photons increased $c_{I_3^-}$ by the reduction process described in Equation 2.15. In the recombination dominated thermal region, equations 2.38 and 2.40 indicated that J_{SC} is proportional with J_{ph} if the recombination current density, J_r, does not significantly change. Increased irradiance will linearly increase the current density of the electrons injected from the dye to the TiO_2 layer, J_{inj}, and thus increase both J_{ph} and J_{SC} [12, 127]. Similar results indicating a linear relationship between J_{SC} and irradiance in the 500 to 1000 W m^{-2} range are reported in other DSSC studies [8, 127]. The positive slope, $\mathrm{d}J_{SC}/\mathrm{d}T$, in the diffusion limited thermal region and its negative counterpart in the recombination limited region are steeper than what was reported by Berginc *et al.* for a DSSC with acetonitrile-based electrolyte.

Figure 3.7(b) displays the relationship between V_{OC} and irradiance at three temperatures. The intensity dependence of open circuit voltage, V_{OC},

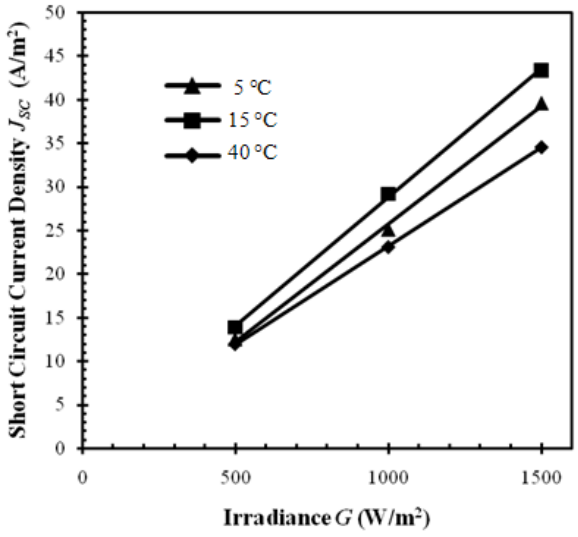

(a)

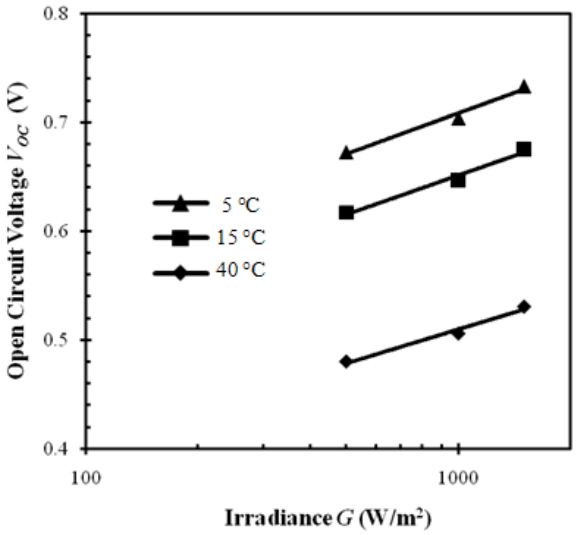

(b)

Figure 3.7: (a) Short circuit current density and (b) open circuit voltage relationships with irradiance at 5, 15, and 40 °C.

was found to be logarithmic. This relationship has been well known to apply to DSSCs and found by previous studies [8, 118, 128]. It is determined by two competing processes [128]. Increased irradiance reduces charge lifetime and will lower V_{OC} [128]. However, increased irradiance will also increase V_{OC} by raising the DSSC chemical potential [125, 128]. The increase resulting from the raised chemical potential is dominant and therefore V_{OC} increased with increased irradiance.

Figure 3.8 illustrates the combined effects of temperature and irradiance on the DSSC photoconversion efficiency, η. Showing influence of J_{SC} on η, two thermal regimes exists with a boundary at 15 °C. At temperatures below 15 °C, efficiency appeared to be independent of temperature. There was an overall decrease in η with increasing temperature at temperatures above 15 °C. This was similar to what also demonstrated by Berginc *et al.* for DSSC with acetonitrile-based electrolyte [29]. The DSSC efficiency increased slightly at higher efficiencies. This was attributed to the higher V_{OC} at higher irradiances across the temperature range. The influence of irradiance on V_{OC} and η was also demonstrated by Huang *et al.* [8].

These results, combined with previous studies, suggest that for future commercialization, the temperature of DSSC modules may require more scrutiny than conventional silicon photovoltaic cells. The photoconversion efficiency of silicon cells therefore exhibit a relatively straightforward, negative relation with temperature in typical operating temperatures (i.e. 5 to 50 °C range) [9, 12]. Due to the two competing temperature dependent process that

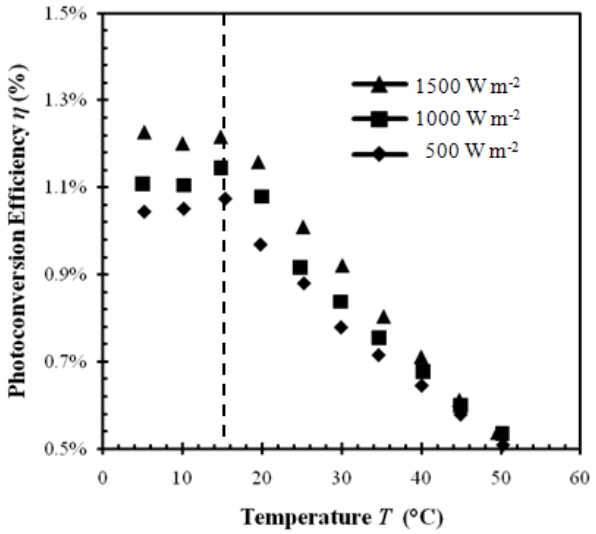

Figure 3.8: (Photoconversion efficiency as functions of temperature from 5 to 50 °C at three irradiances 500, 1000, and 1500 W m^{-2}.

determines DSSC photoconversion efficiency, optimum operational temperature can vary and be tuned. In our current study, an liquid acetonitrile containing a typical I_2 concentration was used and the optimum efficiency at 1000 W m^{-2} was 15 °C. DSSCs with the ionic liquid-based electrolytes, possessing lower efficiencies but with higher stability than acetonitrile-based electrolytes, has different optimum temperatures. Previous ionic-liquid based DSSCs reached maximum η at temperatures between 10 and 40 °C [29, 109, 116]. These different optimum temperatures may meant different temperature dependencies of the recombination rate k_r. DSSC commercialization may entail optimizing DSSC modules for use in specific temperature regimes.

Chapter 4

Conclusions and Recommendations

This study reports the fabrication and characterization of dye sensitized solar cells with acetonitrile based electrolyte. The coupled thermal and irradiance dependent current-voltage characteristics and photoconversion efficiency were measured under varying irradiance from 500 to 1500 W m^{-2} and operating temperatures from 5 to 50 °C. Based on the obtained results the following conclusions can be drawn:

1. For all irradiances two thermal performance regions are defined. At temperatures lower than 15 °C the short circuit current increased with increasing temperature indicating recombination process limited by electron density. At temperatures larger than 15 °C the short circuit current decreased with increasing temperature indicating electron transfer-limited recombination.

2. The short circuit current increased linearly with increasing irradiance. Moreover, at temperatures where short circuit current was relatively larger, it was more sensitive to changes in irradiance.

3. For all irradiances the open circuit voltage decreased linearly with increasing temperature.

4. For all temperature the open circuit voltage increased logarithmically with increasing irradiance. The sensitivity of the open circuit voltage to irradiance was similar at all temperatures.

5. The photoconversion efficiency of the cells was not significantly affected by temperature at temperatures smaller than 15 °C. At larger temperatures the efficiency decreased with increasing temperature.

6. The photoconversion efficiency increased with irradiance and was more sensitive to irradiance at lower temperatures.

The data obtained in this study can be useful for mathematical modeling of charge separation, recombination and ion diffusion phenomena in DSSCs for better understanding and optimizing the design of DSSCs for maximum performance under varying operating conditions.

Moreover, this study promoted the following topics for further research to develop robust and highly efficient dye sensitized solar cells:

1. Mathematical modeling of DSSCs taking into account photon transport and absorption, charge separation, transport and recombination and ion diffusion as functions of irradiance and temperature. The model can be used to vary design parameters such as geometry and material properties to design highly efficient cells under wide range of operating conditions.

2. A common method of recombination suppression for DSSCs is the addition of nitrogen heterocyclic compounds (NHCs) in liquid electrolytes

[125]. Current-voltage (IV) characterization of DSSCs with different NHC concentrations over a wide range of temperature and irradiance can determine the optimum concentrations of NHCs for DSSCs.

3. Lastly, this study promotes experimental and computational studies of the viability of DSSCs in concentrated solar power systems. These systems seeks to lower costs by concentrating the irradiance of an incident area larger than that of the solar cell [130]. Both the operating temperature and irradiance experienced by photovoltaic cells are very high [130]. Determination of the short and long term IV characteristics under high irradiance and temperature are required to improve efficiency and stability of DSSCs in concentrated solar power systems.

Appendices

Appendix A

External and Internal Quantum Efficiency Measurements

The setup and operation of the quantum efficiency measurement system for photovoltaic cells is described in this appendix.

A.1 Optical Alignment and Collimation

The first step to conducting a quantum efficiency (QE) measurement is to optically alignment the instruments for subsequent reference and photocurrent measurements. These are the steps for alignment of the EQE measurement system:

1. Begin the spreadsheet "QE Measurement" and save a new copy. Plug in and roughly visually aligned all instruments. Use the level and angle finder to level the lamp, monochromator, and optics breadboard. To adjust the height of each equipment, rotate the four screws located at each corner. Remove the two red protective covers from the input and output ports of the monochromator (Newport, Cornerstone 260, CA, USA). Tape the paper target onto the Silicon (Si) detector (Hamamatsu, S1336-8BK, Japan) so that the circular flange of the detector is inscribed

within the square target. The Si detector is installed onto a optical rail on the optical breadboard

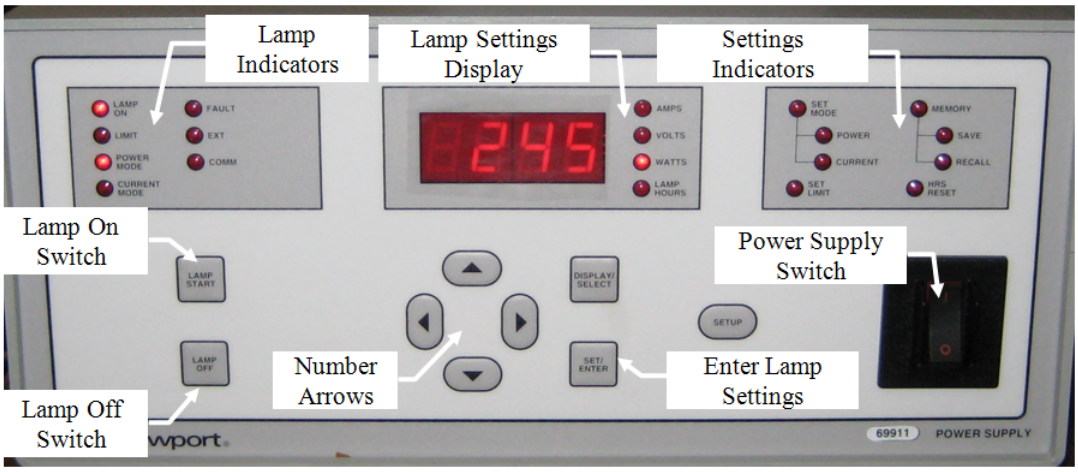

Figure A.1: Lamp power supply at "lamp on" setting.

2. The intensity of the 300 W Xe lamp (Newport, 66984, CA, USA) presents a danger to the experimenter. Make sure the laser safety glass (Newport, G3984, CA, USA), lab coat, nitrile or latex gloves are worn before igniting the lamp. The lamp power supply (Newport, 69911, CA, USA) is shown in Figure A.1. Turn it on with the power switch. The lamp settings display shows the amount of power which will be supplied to the Xe lamp. According to manufacturer regulations, the Xe lamp can be supplied with power from 240 to 360 W. The intensity of the incident light is proportional to supplied power. Press SET/ENTER and use the four arrows to change the power setting. Press the LAMP START button to ignite the Xenon lamp. The intensity of the lamp steadily de-

creases over an hour until it reaches steady. It is recommended to begin measurements after this period.

3. Next, the output monochromatic light is aligned and collimated. Start the "QE System" LabVIEW VI. Turn on the monchromator. Run QE Measurement and select a wavelength in the visible region, such as 400 nm in the numerical control box above the GO TO WAVELENGTH button. Press GO TO WAVELENGTH and the monochromator will select that wavelength, displaying the current wavelength under CURRENT WAVELENGTH. Press END PROGRAM TO stop the VI. The bandpass of the output monochromatic light is determined by the reciprocal dispersion, the ratio of the bandpass to outlet slit width, of the current grating. Adjust the micrometer-driven output slit to vary the bandpass. Enter the selected slit width in the "Monochromator" tab of the spreadsheet. Finally, measure the distance between the Si detector flange and the tip monochromator output lens assembly.

4. Using the target, iteratively adjust the position of the Si Detector until a rectangular, collimated beam is present at the center of the paper target. Using the digital caliper, measure rectangular beam image to confirm that the dimensions are less than 5.80 $\times$ 5.80 mm-the area of the sensitive photoanode in the Si detector. Insert the OD = 1.0 neutral density filter (Thorlabs, NJ, USA) and use another paper target to ensure the monochromatic beam travels through the center of the filter.

A.2 Reference Spectral Irradiance Measurement

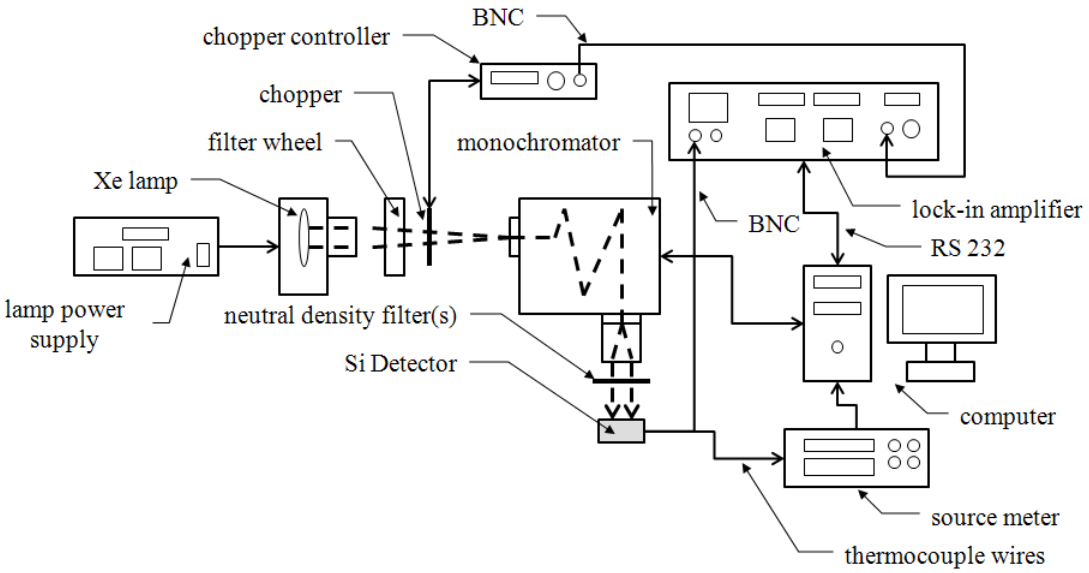

Figure A.2: Schematic of quantum efficiency measurement system for photovoltaic cell spectral photocurrent measurement.

The first measurement using the EQE system is of the reference incident spectral irradiance, G_λ. Figure A.2 shows a schematic of the QE system during a reference measurement. These are the steps to conduct the reference measurement:

1. Remove the paper target from the Si detector. Connect the Si detector to the lock-in amplifier (Stanford Research Systems, SR830, CA, USA) using BNC cable, as shown in Figure A.3. Connect the optical chopper controller, shown in Figure A.4 and power supply (Stanford Research Systems, SR540, CA, USA) to the lock-in amplifier, also via BNC cable.

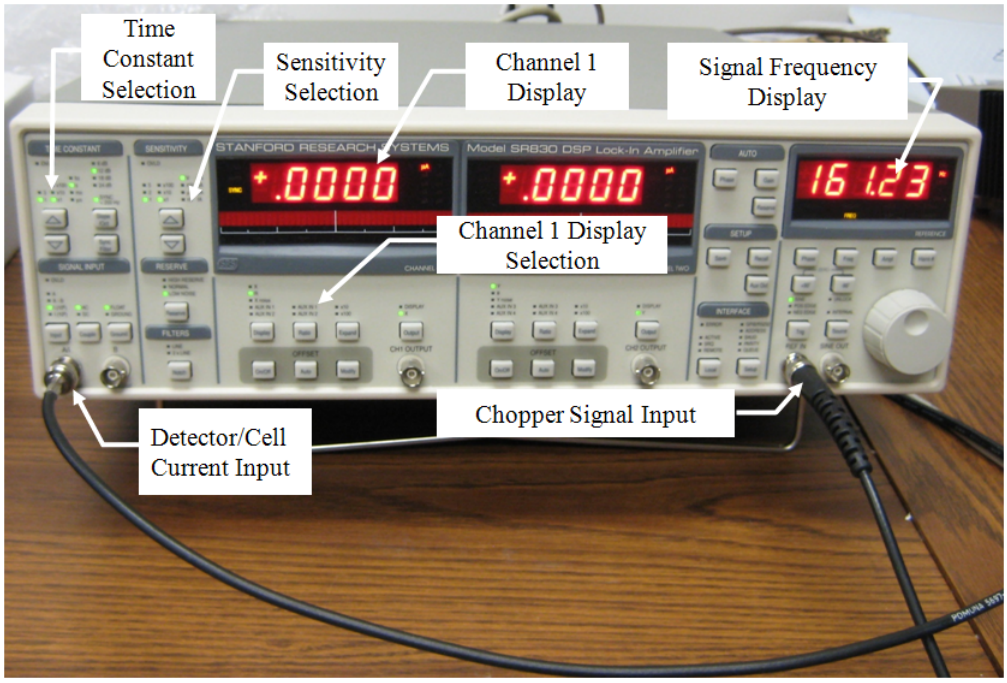

Figure A.3: Lock-in amplifier during EQE operation.

2. Turn on the lock-in amplifier. Select the following settings:

   - Time Constant = 100 ms
   - Slope = 24 dB
   - Sensitivity = 1 μs
   - Channel 1 Display = R
   - Input = I (10^6); AC

3. Turn on the optical chopper and select a frequency using the range selector and control knob on the chopper controller and power supply. The recommended frequency is between 100 to 200 Hz. Frequencies at or a

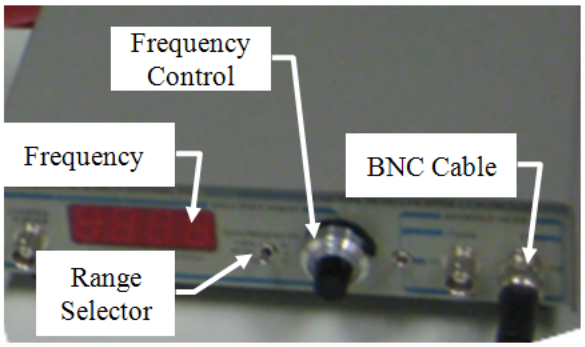

Figure A.4: Chopper controller and power supply.

few Hz adjacent to a multiple of 60 Hz, e.g. 120 Hz, must be avoided.

4. Run the QE System LabVIEW VI. On the control panel, select the range of the scan by entering the beginning wavelength under START WAVELENGTH and the stopping wavelength under END WAVELENGTH. The maximum range detectable by the Si Detector is 300 to 1100 nm. Select the scan's intervals under WAVELENGTH INTERVAL and the number of measurements at each interval under MEASUREMENT PER INTERVAL. More measurements per interval ensure higher accuracy and shows the precision of the final spectral irradiance measurements. The MEASUREMENT DELAY is the time between changing to the new wavelength and the first measurement, as well as the time between each subsequent measurement. This delay is typically optimum at 10 to 20 s, depending on the capacitance of the photovoltaic cell to be tested. Cells with higher capacitance, like DSSCs, require longer delays.

5. To store data, press TURN ON SAVE. Press START SCAN to begin

scanning. A windows dialogue box will put up to prompt the location and name of the data file. Enter the file name like this: filename.txt. The scan will commence. The current wavelength is displayed under CURRENT WAVELENGTH and the current channel 1 R value, the Si detector's current, is displayed under CURRENT R VALUE. After the scan is finished, press END PROGRAM.

6. Go to the folder and open the data text file. Each line contain the data measured at each interval, the wavelength, R value (current), the R value standard deviation, and R value standard error, separated by semicolons. Go the "Irradiance" tab of the spreadsheet. With the cell A2 selected, copy the saved data. In the options for the pasted data, choose separation by semicolons. The spreadsheet "Irradiance" calculates and graphs the power, irradiance, and spectral irradiance from the data.

A.3 Photovoltaic Cell Spectral Photocurrent Measurement

Next, the spectral photocurrent of the photovoltaic cell is measured:

1. Carefully disconnect the Si detector from the BNC cable and the breadboard. Install the photovoltaic cell so that it is at the same distance from the tip of the monochromator outlet lens assembly as the Si detector. Use the BNC-banana clip adaptor to connect the photovoltaic cell with the lock-in amplifier.

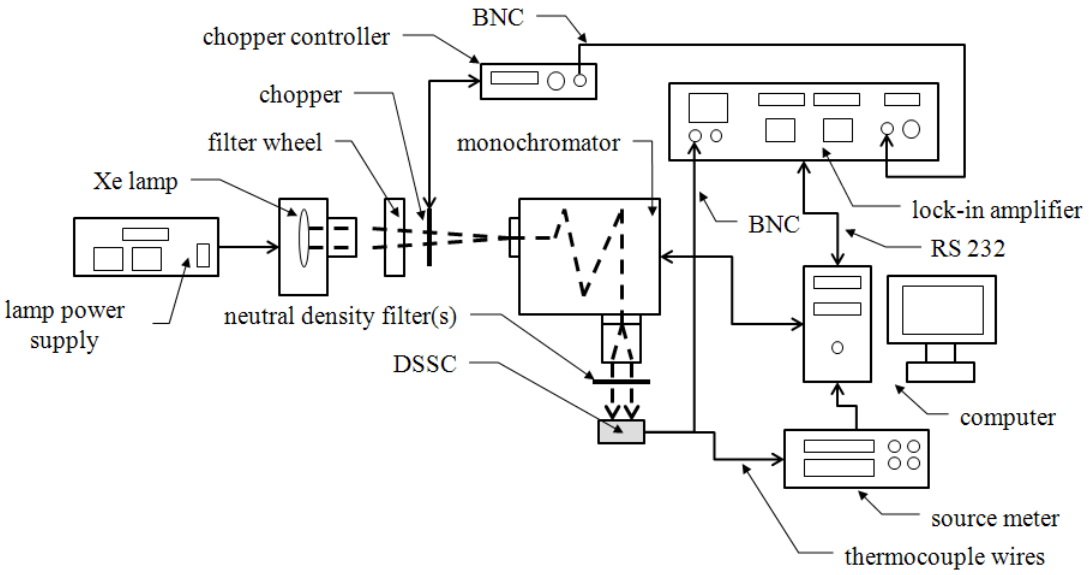

Figure A.5: Schematic of quantum efficiency measurement system for photovoltaic cell spectral photocurrent measurement.

2. Run a scan using the same settings for the QE System LabVIEW VI and lock-in amplifier as was used for the reference spectral irradiance measurement.

3. Copy and paste the data file into cell A2 on the "Cell" sheet of the spreadsheet. The cell's photocurrent is graphed.

A.4 Transmittance and Reflectance Measurements

The transmittance and reflectance of the photovoltaic cell's photoanode is used to determine internal quantum efficiency (IQE). It is determined in this way:

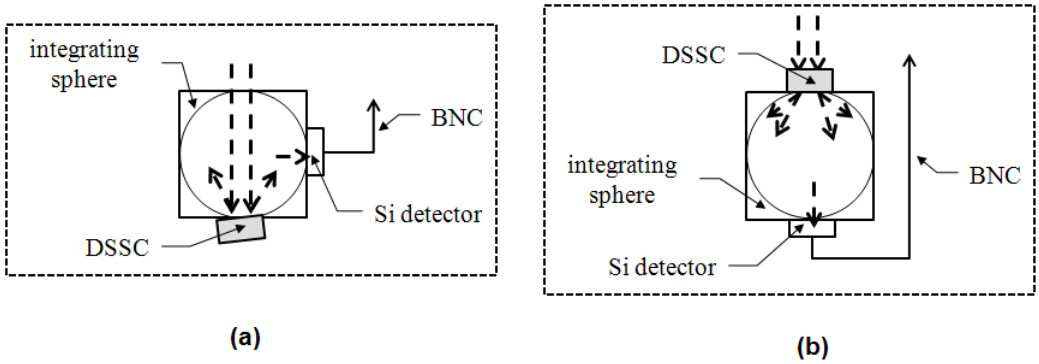

Figure A.6: Configuration of the integrating sphere and Si detector for (a) transmittance and (b) reflectance measurement.

1. The integrating sphere (SphereOptics, SPH-4Z-4, NH, USA) is prepared with installed Si detector in the manner of a transmittance or reflectance measurement as show in Figure A.6. The integrating sphere will be installed in place of the rail on the optical breadboard.

2. Temporary tape the paper target over the inlet port of the integrating sphere. Visually align the integrating sphere so that a collimated, rectangular beam image appears through the center of the inlet port.

3. Conduct a reference and sample measurement using the same LabVIEW VI and lock-in amplifier settings as was used for the spectral irradiance and cell photocurrent measurements. In the case of transmittance, the reference measurement is conducted without any object covering the inlet port. The sample measurement is conducted by taping the photoanode over the inlet port so that the monochromatic light passes through the photoanode. In the case of reflectance, the reference measurement is

taken with a port plug as the tested sample. The sample measurement substitutes the photoanode for the plug.

4. Copy and paste the reference and sample measurements in the "Transmittance" and "Reflectance" tabs of the spreadsheet. The spectral transmittance and reflectance is calculated.

A.5 Quantum Efficiency Data Analysis

The external (EQE) and internal (IQE) quantum efficiency and sensitivity are calculated in the "EQE" and "IQE" tabs of the spreadsheet. Comparisons of the tested cell can be made with other cells in the "Comparison" tab.

Appendix B

Polarization Curve Characterization

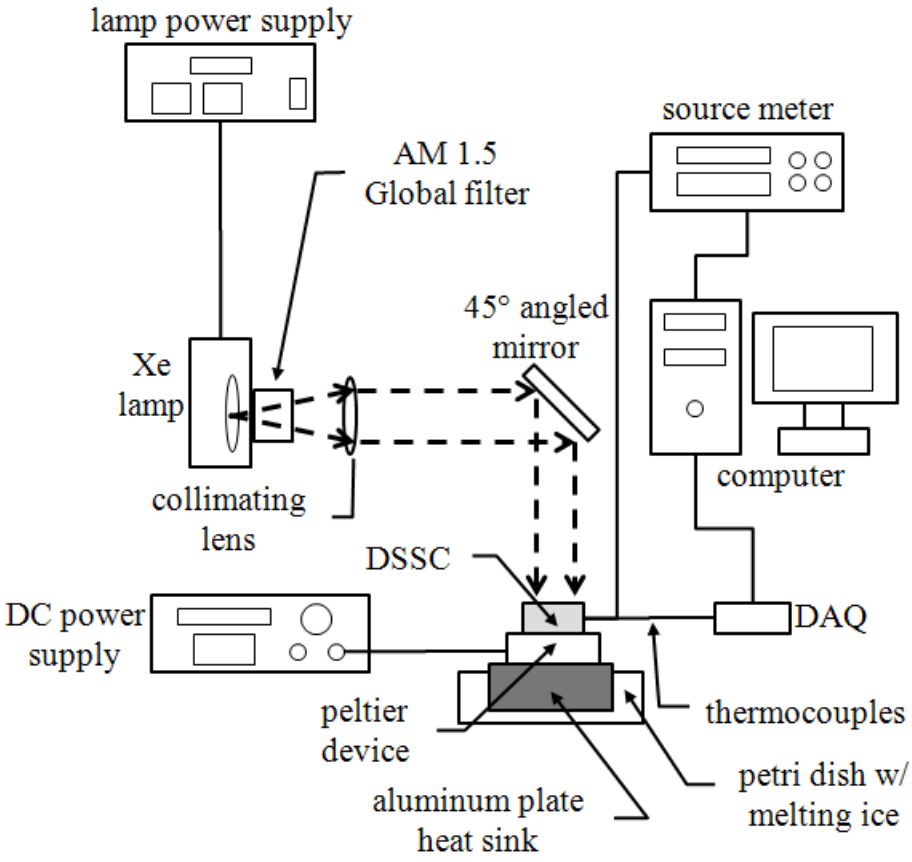

Figure B.1: Schematic of the temperature controlled photovoltaic cell polarization curve measurement system.

The polarization, or current-voltage (IV), curve of dye-sensitized solar

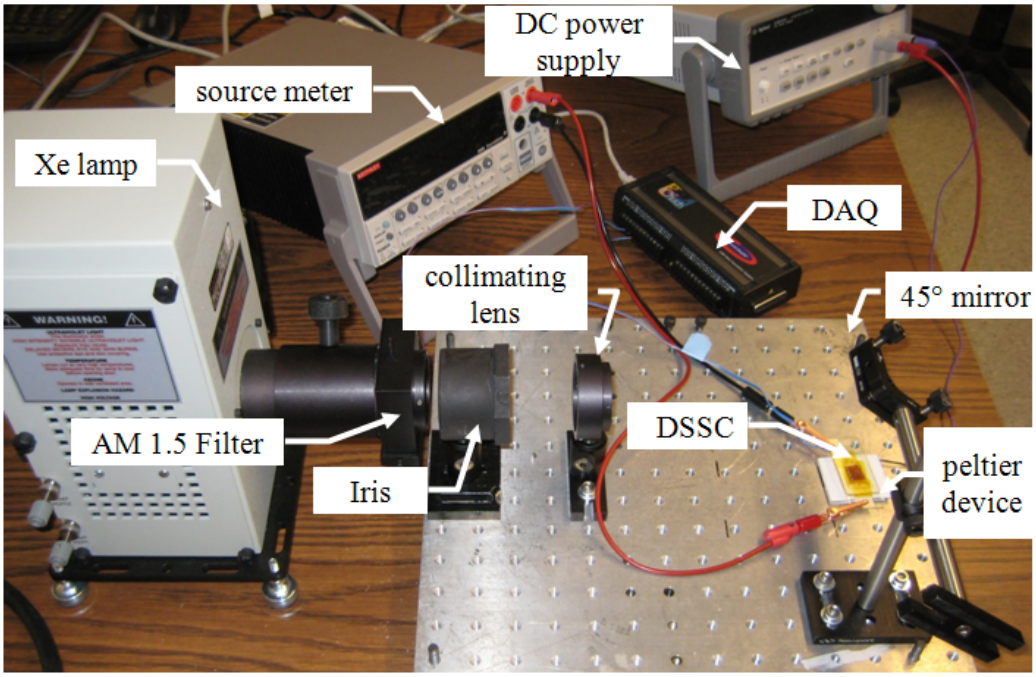

Figure B.2: Photograph of the polarization curve characterization system.

cells (DSSCs) are measured using an isothermal polarization curve measurement system. Figure B.1 is the schematic and B.2 is a photograph of this system. The operation of this system is divided into the use of a source meter (Keithley, 2400, OH, USA) to measure the IV curve, detailed in Section B.1, and control of the photovoltaic cell's temperature, described by Section B.2. Section 2.4.1 explains the definition and use of the IV curve for photovoltaic cells.

B.1 Source Meter Characterization

These are the steps for measurement of the IV curve of a photovoltaic cell is measured using a Keithley 2400 source meter:

1. Open and save a new version of the Excel spreadsheet "IV Measurement". Install the AM 1.5 Global filter (Newport, CA, USA) onto the Xe lamp holder. Visually align the Xe lamp with the neutral density filter holders.

2. Turn on the Xe lamp taking the same precautions and following the same steps as described in the QE measurement system section. Use the light blocker to trap the incident light.

3. Connect the NREL calibrated silicon photovoltaic reference cell (Hamamatsu, S1133A KG5 Filtered, Japan) to the souce meter. Align the cell so that at the same location as the photovoltaic cell and incident to the light. Press the "I" button on the "Measure" panel and the "V" button on the "Source" panel on the source meter to measure the cell's short circuit current, I_{SC}. The reference cell produces a I_{SC} of 0.747 mA at an irradiance, G, of 1000 W m^{-2}. The I_{SC} is assumed to have linear response to G over the range of 500 to 1500 W m^{-2} at room temperature, e.g. I_{SC} is 0.374 mA at G of 500 W m^{-2} [12]. Use a combination of different neutral density filters and adjusting lamp power to select the irradiance level. Measure the irradiance at before, during, and after each IV curve measurement, as the output of the Newport Xe lamp can vary

about ± 2%. Enter the calculated irradiance levels in the "Irradiance" tab of the "IV Measurement" spreadsheet to find an average G value of the IV for use in calculating solar conversion efficiency via Equation 2.30.

4. Connect the photovoltaic cell with the source meter. Run the LabVIEW VI "2400 swA Linear Stair with DCV". Enter the starting voltage in START V, ending voltage in STOP V, and the number of data points in POINTS. Select 1.000E-2 for COMPLIANCE I, 1 for ARM COUNT, 0.01 for NPLC, 2 s for TRIG DELAY, and 3 s for SOUR DELAY. Press SETUP LINEAR STAIR SWEEP to confirm your settings. The voltage interval is displayed in STEP V. Choose YES for LOG. Under FILE PATH, specify the location and name of the data file.

5. To start the IV measurement, press START SWEEP. The data, voltage and corresponding current, is displayed in the DATA tab, GRAPH tab, and stored in the saved data file.

6. Copy and paste the data file into cell A2 of the "IV" in the spreadsheet. Enter the area of the cell's photoanode in "Settings" tab.

7. The current density, J, voltage, and power is plotted as IV and power curves. Using an equation solver, such as Matlab, the maximum power density can be determined. Entering that information in the "Analysis" tab will provide fill factor (FF) and photoconversion efficiency (η).

B.2 Temperature Control

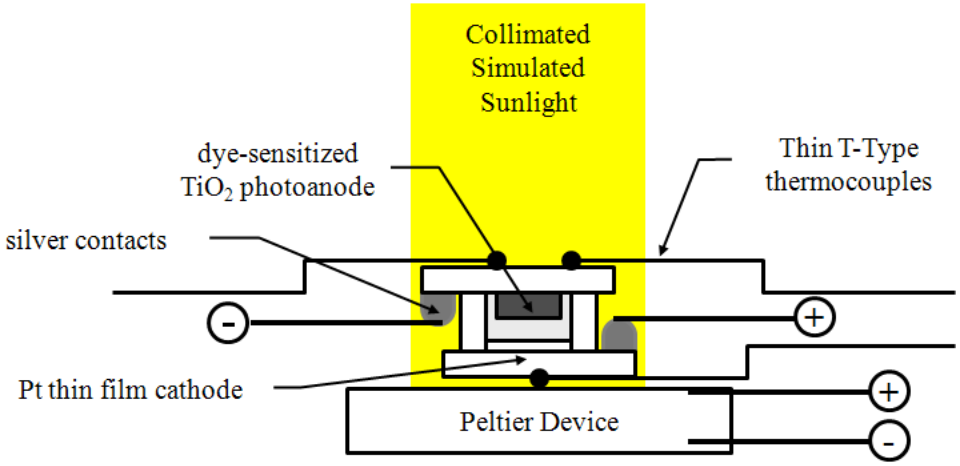

Figure B.3: Side schematic of a DSSC.

The temperature of the photovoltaic cell can be maintained from 5 to 100 °C using the temperature control apparatus:

1. Tape the tips of T-type thermocouples (Omega, TT-T-36-100, CT, USA) onto both sides of the photovoltaic cell using heat resistant tape (Fisher Scientific, 19-160-0098, USA), as shown for a DSSC in Figure B.3. Use a flathead screw driver to connect the ends of each thermocouple to the analog ports of the data acquisition device (DAQ). Increase the number of thermocouples to increase the accuracy of cell temperature measurements. If the temperature readings on both sides of the cell is within 1 °C, the temperature is assumed constant throughout the cell and is determined by the mathematical mean of all thermocouple readings.

2. The front of the Peltier device (Marlow, RC12-8-01, TX, USA) is attached to the back of the photovoltaic cell using zinc oxide conductive thermal paste (GC Electronics, 10-8106, IL, USA) and clamps. Squeeze an approximately 10 mm diameter drop of thermal paste onto the Peltier device's front (the side with lettering) face. Spread the paste into an even film with a metal spatula. Press the back side (opposite to photoanode) of the photovoltaic cell onto the Peltier device's front face.

3. Connect the Peltier device to the DC power supply (Agilent, E3642A, CA, USA). To heat the front surface, connect the positive terminal of the Peltier device to the positive terminal of the power supply and the negative to the negative.

4. Reverse the polarities to cool Peltier device's front surface. Place the Peltier device w/ the attached cell on the aluminum block heat sink w/ thermal paste, as shown in Figure B.1. The heat sink is cooled by partially submerging in a petri dish of melting ice water.

Appendix C

Thin Film Characterization

The nanocrystalline TiO_2 thin films utilized in this study's photoelectrochemical cells are characterized for their electrical and physical properties. Section C.1 contains instructions for using the four point probe method to characterize the sheat resistance and sheat resistivity of the thin films. Surface imaging of the thin films using a scanning electron microscope (SEM) is described in Section C.2. Lastly, Section C.3 discusses measurement of thin film thickness using a profilometer.

C.1 Four Point Probe Characterization

The four point probe apparatus measures the sheet resistance and sheet resistivity of thin films using the van der Pauw method. Theoretical considerations of sheet resistance and sheet resistivity are discussed in details in Section 2.3. These are the instructions for sheet resistance and sheet resistivity measurements of thin films used in this study:

1. Install the thin film into the sample holder as seen in Figure C.1. The sample can have a maximum thickness of 10 mm and have a projected area no larger than a 25 mm by 25 mm square. Carefully pull each gold

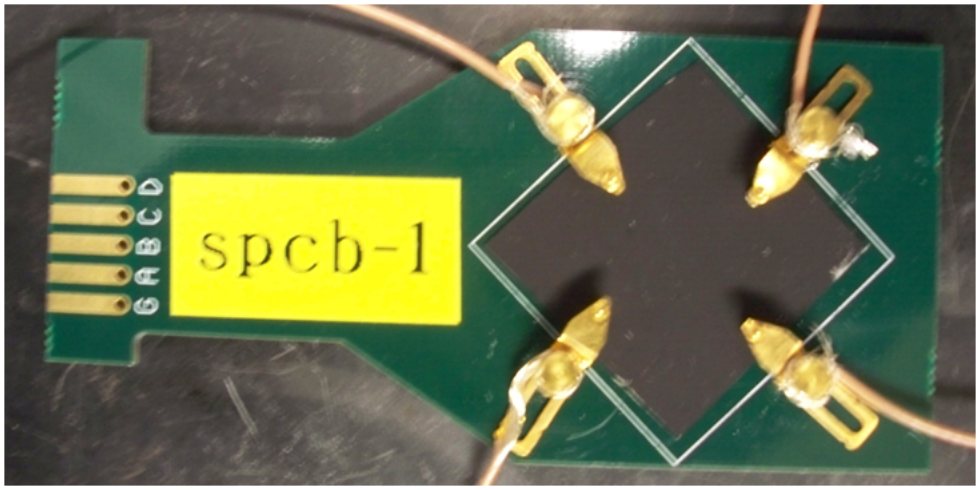

Figure C.1: A sample, a black carbon film, is held by the four probes during resistivity measurement.

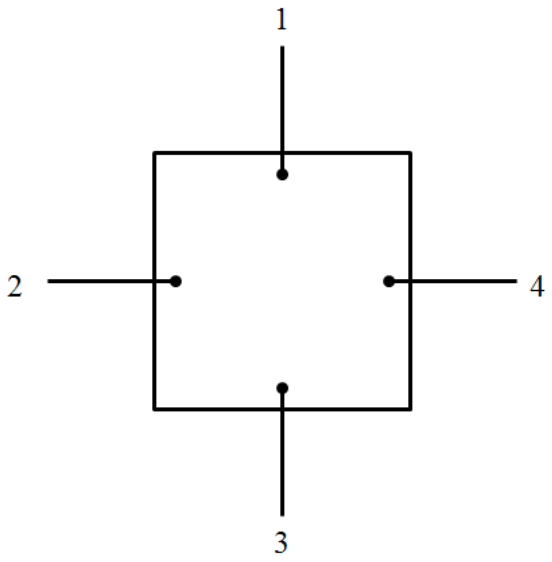

Figure C.2: Schematic of connections on a sample undergoing conductivity testing by a four-point probe utilizing van der Pauw method [10, 11].

plated pin and gently release the pin over a point on the film. Identify the four pins so that they are arranged as shown in Figure 2.6.

2. Turn on the multimeter (Keithley, 2400, OH, USA) and select Source I, Measure V, and four point test. Run the LabVIEW VI "2400 swA Linear Stair with DCV". In the Scan settings, choose to source current from -1 mA to +1 mA at 50 μA intervals. Enter -0.0001 in START A, +0.0001 A in ending voltage in STOP V, and 41 for number of data points in POINTS. Select 1.000E+2 for COMPLIANCE V, 1 for ARM COUNT, 0.01 for NPLC, 1 s for TRIG DELAY, and 1 s for SOUR DELAY. Press SETUP LINEAR STAIR SWEEP to confirm your settings. The current interval is displayed in STEP I. Choose YES for LOG. Under FILE PATH, specify the location and name of the data file.

3. Start the first, "vertical edge", resistance measurement. Connect the wires leading from point 1 and 2 to the left column of the red and black input ports respectively at the front of multimeter. Connect the points 3 and 4 to the right column of red and black input ports, respectively.

4. Press START SWEEP to begin scan. The data, current and corresponding voltage, is displayed in the DATA tab, GRAPH tab, and stored in the saved data file. Copy and paste the data into "Configuration 1" section of the Excel worksheet "Conductivity Template". The sample's R_v is the average of all R_v calculated at each current and voltage measurement using Equation 2.25.

5. Start the "horizontal edge" resistance measurement. Connect the wires leading from point 2 and 3 to the left column of the red and black input ports respectively at the front of multimeter. Connect the points 4 and 1 to the right column of red and black input ports, respectively.

6. Press START SWEEP to begin scan. The data, current and corresponding voltage, is displayed in the DATA tab, GRAPH tab, and stored in the saved data file. Copy and paste the data into "Configuration 1" section of the Excel worksheet "Conductivity Template". The sample's R_h is the average of all R_h calculated at each current and voltage measurement using Equation 2.26.

7. The sheet resistance is calculated using formula 2.24. The film thickness measurement from Section C.3 is used to calculate the resistivity of the film using equation 2.23.

C.2 Scanning Electron Microscopy Characterization

The surfaces of the nanocrystalline anatase titanium(IV) dioxide (TiO_2) thin films were characterized by a scanning electron microscope (SEM). The preparation of thin film samples is detailed in Section C.2.1. The instructions for surface imaging of the samples by a SEM (FEI, F600, OR, USA) is described in Section C.2.2.

C.2.1 Sample Preparation

The preparation of a nanocrystalline TiO_2 thin film for SEM characterization is described:

1. Deposit the TiO_2 thin film onto center of the conductive side of a fluorine-doped tin oxide (FTO) glass plate (Hartford, TEC-8, IN, USA) measuring 25×25×3.2 mm. The deposition method will be identical to what would be used to fabricate the thin film for an actual photoelectrochemical cell used in this study; different deposition methods will produce thin films with different structures. The thin film area is limited to smaller than 25×25 mm in order leave room on the plate's conductive surface for electrical contact.

2. Deposit a layer of silver conductive epoxy (MG Chemicals, 8331-14G, Canada) onto the edges of the conductive surface. Use the doctor-blade method with one layer of 50 μm thick tape (3M, Tape 810, MN, USA). There should be at least 3 separate areas of the silver layer, each with an minimum area of approximately 25×25 mm. This is to confirm electrical contact with the SEM sample holder.

3. Test the resistance of the sample. Turn on the handheld multimeter (Omega, HHM29, CT, USA) to resistance measurement mode by turning the function/range switch to the notch indicated by the resistance "Ω" symbol. Press the contacts of the multimeter's lead wires onto sample's silver conductive epoxy film, with each contact on opposite sides of the

sample. The resistance measurement should preferably be lower than 10 Ω for good imaging with SEM.

C.2.2 Surface Imaging

These are the instructions for using the Quanta FEG SEM for surface imaging of a nanocrystalline TiO_2 thin film [131]:

1. Mount the thin film sample onto the 32 mm diameter polished specimen holder with three copper clips. Place the sample with the conductive surface facing upwards on the center of the specimen holder. Use a screwdriver to clamp the sample with the three copper clips so that each clip is securely attached on top of the silver conductive epoxy layer.

2. Test the resistance of the sample. Turn on the handheld multimeter (Omega, HHM29, CT, USA) to resistance measurement mode by turning the function/range switch to the notch indicated by the resistance "Ω" symbol. Press one contacts of the multimeter's lead wires on the surface of the specimen holder away from the clamped sample and the other contact onto empty section of the FTO conductive surface. The adequate resistance measurement for SEM imaging is preferably less than 15 Ω.

3. Turn on the nitrogen gas supply to a pressure of 7 psi and press Vent button on Vacuum module of the Quanta FEG computer control interface to vent the SEM sample chamber. The Vacuum Status icon below

the Vent button will turn orange until the chamber is fully vented, then the icon will turn grey.

4. Open the chamber door and carefully place the specimen holder into the sample holder in the middle of the chamber. Use latex gloves at all times when placing and removing samples to avoid sample chamber contamination.

5. Close the chamber door. Select the High Vacuum setting on the Vacuum module and press the Pump button. The Vacuum status icon will turn orange until the sample chamber reaches the maximum allowable pressure under High Vacuum mode, when it will turn green.

6. Press Beam On in the column module to turn on the electron beam and begin imaging. Select 3.0 as the Spot size and a voltage of 30.00 kV. On the Magnification module, set 50X magnification.

7. Dragging around the mouse while keeping the left button pressed on the image window to center on the thin film. In the Tools Menu, select Auto Contrast Brightness, Auto Stigmator, and Auto Focus, respectively, to form a fairly focused image of the thin film.

8. Increase magnification to 50,000X to 150,000X to resolve the nanostructure of the thin films. Focus the image using the Auto Focus button. If the image remains blurry and the nanostructures, such as the interconnected anatase TiO_2 particles in a sol-gel deposited thin film, cannot

be resolved, the stigmatism of the electron beam requires adjustment. Select Auto Stigmator again in the Tools menu. If image remains blurry, perform "manual" stigmatism adjustment by slowly dragging the Stigmator 2D control until image quality improves.

9. To save an image, first select the highest resolution, 4096X3536, available from the Screen Pixel Resolution List Box. Next, select Save in the Tools Menu. Choose the location where the image is desired and select the TIF 24 or BMP 24 file type.

10. Press Vent button to vent the sample chamber. Once again, the Vacuum Status icon will turn orange, then grey once the chamber is fully vented. Open the sample chamber to remove the specimen holder. Close the chamber door, select High Vacuum mode, and press Pump. Wait until the Vacuum Status icon reaches green. Turn off the nitrogen gas supply. Remove the test sample from the specimen holder.

C.3 Profilometer Characterization

In this study, the Dektak 6M profilometer at the Center for Nano and Molecular Science and Technology of The University of Texas at Austin is used to measure the thicknesses of the nanocrystalline TiO_2 thin films. These are the instructions for using the profilometer (Dektak, 6M, NY, USA) [13]:

1. Prepare a TiO_2 thin film for the profilometer sample using the same methods as for the actual photoanodes. Deposit the TiO_2 thin film

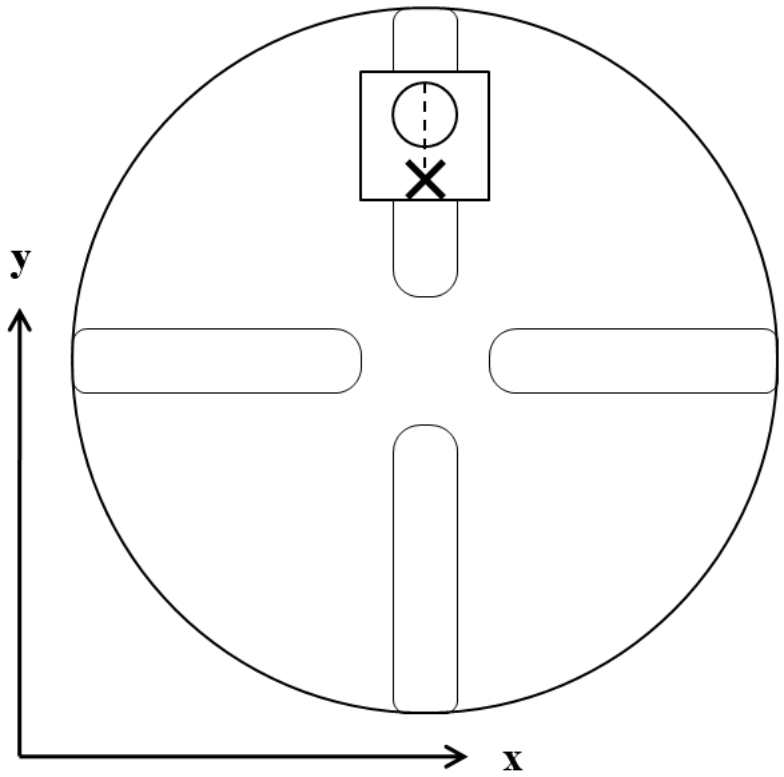

Figure C.3: Schematic of the profilometer's circular sample stage showing the position of a circular thin film on the square FTO glass plate with the cross indicating starting position for profilometer scan [13].

on a fluorine-doped tin oxide (FTO) glass plate (Hartford, TEC-8, IN, USA) measuring 25×25×3.2 mm. In order to provide sufficient area for baseline thickness measurements, the area of the thin film must not be larger than half the area of the plate.

2. Turn on the Dektak 6M software. Select Tower Up in the Profiler menu to raise the profilometer's stylus and the optics tower. Place the sample on the sample stage of the profilometer as shown in Figure C.3. Select

the direction and location for the stylus to move through the thin film. Orient the sample by taking account the fact that during a profilometer scan, the stylus moves in the positive Y axis.

3. Press the Sample Positioning button to bring up the Sample Positioning Window. Select Tower Down in the Profiler menu to lower the Profilometer's stylus and the optics tower. The Sample Positioning Windows displays a live magnified image of the stylus and the area on the sample stage adjacent to it.

4. Manually adjust the position of stage so that the stylus is located at the starting point of a profilometer scan. Figure C.3 shows a sample scan, indicated by the dotted line, through the thin film that has a starting point in the empty area of the glass plate, denoted by the cross. The starting point, indicated by the cross, must be on an empty area of the glass plate that is a minimum distance of 2 mm in the negative Y axis direction away from the thin film. Use a hand on each of the X-Y positioning knobs to move the stage. Turn the Left Knob clockwise to move the stage in the positive X direction; turn counterclockwise to move the stage in the negative X direction. Clockwise turning of the Right Knob moves the stage in the positive Y direction away from the operator, while counterclockwise turning move the stage in the negative Y direction toward the operator. Use the live image and crosshairs of the Sample Positioning Window for assistance.

5. Set the parameters for the profilometer scan by selecting Scan Routine in the Window menu to bring up the Scan Routines Window. Press the SCAN PARAMETERS button to bring up the Scan Parameters dialog box. Enter the following settings:

    - Length = dependent on sample-maximum possible scan length of 30,000 μm
    - Resolution = 1 μm per sample - refers to horizontal resolution
    - Duration = $\frac{Length}{Resolution \times 300}$
    - Stylus Force = 3 mg
    - Measurement Range = 2620 k$\mathring{A}$ refers to vertical range
    - Profile = Hills & Valleys

6. Close the sample chamber door. Press SCAN to begin the scan routine. Monitor the scan progress with the live video feed in the data plot screen and confirm that the scan's length and direction are correct.

7. The scan profile screen is displayed after the scan is completed. Figure C.4 shows a typical scan profile of a nanocrystalline TiO_2 thin film of the dye-sensitized solar cells (DSSCs) used in this study. The horizontal axis of the scan profile plot is scan length and the vertical axis is height. The scan started in an area of the glass plate without the thin film, therefore the scan profile began as a linear line, as shown by the left green arrow. The surface of the glass plate is smooth relative to that of the thin film.

Then, the scan profile, the portion indicated by the blue arrows, displays the relative increase in height as the stylus encounters the thickness of the thin film. The scan profile ends with another linear line as the stylus moves beyond the thin film, indicated by the right green arrows. Select Save As from the File menu and choose the "txt" option to save the scan profile data as an exportable text file.

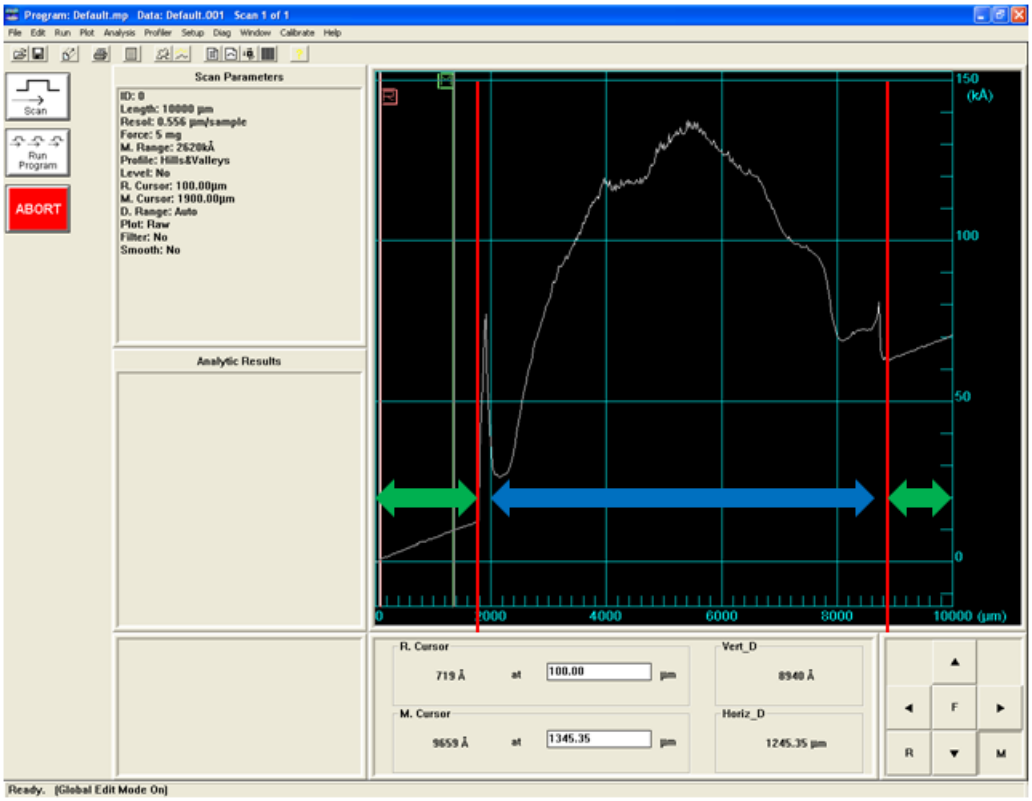

Figure C.4: Screenshot of a sample scan profile plot produced by the Dektak 6M Software. The red lines separate the empty FTO glass plate portions, indicated by green arrows, and the TiO_2 thin film portion indicated by the blue arrow [13].

8. The linear line portions of the scan profile ideally should be straight, as all sections of the empty glass substrate should indicate zero height. This occurs as the glass substrate is not perfectly level with the stylus. Use the Excel spreadsheet "Profilometer Format" with the saved scan profile data to correct for this unlevelness. Enter the data points from the empty glass plates under the Reference section of the Scan tab. Assuming a linear fit due to flat glass plate, the formula to correct the plot into a straight line with zero height is calculated. The data points of the scan profile over the thin film is entered into the Measure section of the Scan tab and is corrected using the same formula. Integrate the resulting plot of corrected height versus horizontal distance using Matlab to calculate the average thin film thickness.

9. Repeat Steps 3-8 for 3 to 4 profilometer scans of different locations across the thin film. Use the Comparison tab of the "Profilometer Format" excel spreadsheet to calculate the average and standard deviation of the thickness measurements.

Appendix D

Nomenclature

The following are the nomenclature used in this thesis:

A	area, m^2
$\mathcal{A}$	optical absorptance, %
A_λ	spectral absorptance, %
c	concentration, m^{-3}
c_0	speed of light in vacuum, $c = 2.998 \times 10^8$ m s^{-1}
D	diffusion coefficient, m^2 s^{-1}
d	distance, m
E	energy, eV
e	elementary charge, $e = 1.602 \times 10^{-19}$ C
e^-	electron
F	Faraday's constant, $F = 9.649 \times 10^4$ C mol^{-1}
FF	fill factor
G	irradiance, W m^{-2}
G_0	solar constant, W m^{-2}
h	Planck's constant, $h = 6.626 \times 10^{-34}$ J s
h^+	electron hole

I	current, A
J	current density, A m^{-2}
k	reaction rate constant, m s^{-1}
k_B	Boltzmann constant, $k_B = 1.3806504 \times 10^{-23}$ J K^{-1}
m	mass, kg
L	Avogadro constant, $L = 6.02214179 \times 10^{23}$ mol^{-1}
N	density, m^{-3}
P	power density, W m^{-2}
Q	activation energy, J mol^{-1}
R	resistance, Ω
R_λ	spectral reflectance, %
$\bar{R}$	universal gas constant, $\bar{R} = 8.314472$ J mol^{-1} K^{-1}
T	temperature, K
T_λ	spectral transmittance, %
t	thickness, m
V	voltage, V
w	width, m

Greek symbols

α	light absorption coefficient #
β	electron recombination transfer coefficient
η	photoconversion efficiency, %
η_s	surface overpotential, V
λ	wavelength, nm

ν	frequency, Hz
Φ	incident photon flux, m^{-2} s^{-1}

Subscripts

A	refers to acceptor
a	refers to activation
CB	refers to conduction band
EQ	refers to external quantum
e	refers to between electrodes
e^-	refers to electron
D	refers to donor
d	refers to dark
f	refers to Fermi level
FB	refers to flat band
g	refers to band gap
h^+	refers to electron hole
in	refers to incident
inj	refers to injected
max	refers to maximum
OC	refers to open circuit
out	refers to output
ph	refers to photocurrent or photovoltage
Q	refers to quantum
$redox$	refers to reduction-oxidation

SC	refers to short circuit
SCR	refers to space charge region
TCS	refers to transparent conductive substrate
TiO_2	refers to TiO_2 film
λ	refers to wavelength or spectral

Superscripts

$*$	refers to excited state

Bibliography

[1] C. R. Nave, "HyperPhysics," 2005.

[2] K. Fredin, "Studies of coupled charge transport in dye-sensitized solar cells using a numerical simulation tool," *Solar Energy Materials and Solar Cells*, vol. 90, no. 13, pp. 1915–1927, 2006.

[3] C. A. Grimes, O. K. Varghese, and S. Ranjan, *Light, Water, Hydrogen*. New York, NY: Springer Science+Business Media, LLC, 2008.

[4] T. Bak, J. Nowotny, M. Rekas, and C. C. Sorrell, "Photo-electrochemical hydrogen generation from water using solar energy. Materials-related aspects," *International Journal of Hydrogen Energy*, vol. 27, no. 10, pp. 991–1022, 2002.

[5] A. B. F. Martinson, T. W. Hamann, M. J. Pellin, and J. T. Hupp, "New architectures for dye-sensitized solar cells.," *Chemistry (Weinheim an der Bergstrasse, Germany)*, vol. 14, no. 15, pp. 4458–67, 2008.

[6] M. Grätzel, "Recent Advances in Sensitized Mesoscopic Solar Cells," *Accounts of Chemical Research*, vol. 42, no. 11, pp. 1788–1798, 2009.

[7] S. a. Haque, E. Palomares, B. M. Cho, A. N. M. Green, N. Hirata, D. R. Klug, and J. R. Durrant, "Charge separation versus recombina-

tion in dye-sensitized nanocrystalline solar cells: the minimization of kinetic redundancy.," *Journal of the American Chemical Society*, vol. 127, pp. 3456–62, Mar. 2005.

[8] S. Y. Huang, G. Schlichtho, A. J. Nozik, M. Gratzel, and A. J. Frank, "Charge Recombination in Dye-Sensitized Nanocrystalline TiO_2 Solar Cells," *Journal of Physical Chemistry B*, vol. 101, no. 14, pp. 2576–2582, 1997.

[9] M. Berginc, U. O. Krasovec, M. Jankovec, and M. Topic, "The effect of temperature on the performance of dye-sensitized solar cells based on a propyl-methyl-imidazolium iodide electrolyte," *Solar Energy Materials and Solar Cells*, vol. 91, no. 9, pp. 821–828, 2007.

[10] L. J. van der Pauw, "A Method of Measuring Specific Resistivity and Hall Effect of Discs of Arbitrary Shape," *Philips Research Reports*, vol. 13, no. 1, p. 9, 1958.

[11] L. J. van der Pauw, "A Method of Measuring the Resistivity and Hall Coefficient on Lamellae of Arbitrary Shape," *Philips Technical Review*, vol. 20, no. 8, p. 5, 1959.

[12] S. C. W. Krauter, *Solar electric power generation - photovoltaic energy systems : modeling of optical and thermal performance, electrical yield, energy balance, effect on reduction of greenhouse gas emissions.* Berlin: Springer, 2006.

[13] Digital Instruments Veeco Metrology Group, *Dektak 6M Manual*, 2002.

[14] J. Halme, P. Vahermaa, K. Miettunen, and P. Lund, "Device Physics of Dye Solar Cells," *Advanced Materials*, vol. 22, pp. 210–234, Aug. 2010.

[15] M. Jefferson, "Sustainable energy development: performance and prospects," *Renewable Energy*, vol. 31, pp. 571–582, Apr. 2006.

[16] K. E. Seiferlein, "Energy Information Administration Annual Energy Review," 2007.

[17] Z. A. Smith and K. D. Taylor, *Renewable and alternative energy resources*. Santa Barbara, CA, USA: ABC-CLIO, 2008.

[18] M. E. Mann, Z. H. Zhang, M. K. Hughes, R. S. Bradley, S. K. Miller, S. Rutherford, and F. B. Ni, "Proxy-based reconstructions of hemispheric and global surface temperature variations over the past two millennia," *Proceedings of the National Academy of Sciences of the United States of America*, vol. 105, no. 36, pp. 13252–13257, 2008.

[19] C. M. Meure, D. Etheridge, C. Trudinger, P. Steele, R. Langenfelds, T. van Ommen, A. Smith, and J. Elkins, "Law Dome CO_2, CH_4 and N_2O ice core records extended to 2000 years BP," *Geophysical Research Letters*, vol. 33, no. 14, 2006.

[20] N. S. Lewis, G. Crabtree, A. J. Nozik, M. R. Wasielewski, and P. Alivisatos, "Basic Research Needs for Solar Energy Utilization," in *Basic Energy*

Sciences Workshop on Solar Energy Utilization, (Bethesda, Maryland), p. 276, Argonne National Laboratory, 2005.

[21] V. M. Andreev, V. A. Grilikhes, and V. D. Rumyantsev, *Photovoltaic conversion of concentrated sunlight*. Chichester ; New York: John Wiley, 1997.

[22] M. Grätzel, "Photoelectrochemical cells," *Nature*, vol. 414, no. November, pp. 338–344, 2001.

[23] S. Chuangchote, T. Sagawa, and S. Yoshikawa, "Efficient dye-sensitized solar cells using electrospun TiO_2 nanofibers as a light harvesting layer," *Applied Physics Letters*, vol. 93, no. 3, p. 3, 2008.

[24] A. F. Nogueira, "Polymers in dye sensitized solar cells: overview and perspectives," *Coordination Chemistry Reviews*, vol. 248, no. 13-14, pp. 1455–1468, 2004.

[25] L.-Y. Lin, C.-P. Lee, R. Vittal, and K.-C. Ho, "Selective conditions for the fabrication of a flexible dye-sensitized solar cell with Ti/TiO_2 photoanode," *Journal of Power Sources*, vol. 195, no. 13, pp. 4344–4349, 2010.

[26] J. Halme, *Dye-sensitized nanostructured and organic photovoltaic cells: technical review and preliminary tests Master's thesis submitted in partial fulfillment of the requirements for the degree of Master of Science*

in Technology Supervisor: Professor Peter Lun. Master of science in technology, Helsinki University of Technology, 2002.

[27] S. Noda, K. Nagano, E. Inoue, T. Egi, T. Nakashima, N. Imawaka, M. Kanayama, S. Iwata, K. Toshima, K. Nakada, and K. Yoshino, "Development of large size dye-sensitized solar cell modules with high temperature durability," *Synthetic Metals*, vol. In Press,, 2009.

[28] V. Suryanarayanan, K.-M. Lee, J.-G. Chen, and K.-C. Ho, "High performance dye-sensitized solar cells containing 1-methyl-3-propyl imidazolinium iodide-effect of additives and solvents," *Journal of Electroanalytical Chemistry*, vol. 633, no. 1, pp. 146–152, 2009.

[29] M. Berginc, U. Opara Krasovec, M. Hocevar, and M. Topic, "Performance of dye-sensitized solar cells based on Ionic liquids: Effect of temperature and iodine concentration," *Thin Solid Films*, vol. 516, no. 20, pp. 7155–7159, 2008.

[30] J. S. Newman and K. E. Thomas-Alyea, *Electrochemical systems.* Hoboken, N.J.: J. Wiley, 3rd ed., 2004.

[31] D. A. Neamen, *Semiconductor physics and devices : basic principles.* Boston: McGraw-Hill, 3rd ed., 2003.

[32] M. Balkanski and R. F. Wallis, *Semiconductor physics and applications.* Oxford ; New York: Oxford University Press, 2000.

[33] J. Nowotny, T. Bak, M. Nowotny, and L. Sheppard, "Titanium dioxide for solar-hydrogen I. Functional properties," *International Journal of Hydrogen Energy*, vol. 32, pp. 2609–2629, Sept. 2007.

[34] W. M. Campbell, A. K. Burrell, D. L. Officer, and K. W. Jolley, "Porphyrins as light harvesters in the dye-sensitised TiO_2 solar cell," *Coordination Chemistry Reviews*, vol. 248, pp. 1363–1379, July 2004.

[35] M. Grätzel, "Dye-sensitized solar cells," *Journal of Photochemistry and Photobiology C-Photochemistry Reviews*, vol. 4, no. 2, pp. 145–153, 2003.

[36] H. Chang, T. Chen, K. Huang, S. Chien, and K. Hung, "Fabrication of highly efficient flexible dye-sensitized solar cells," *Journal of Alloys and Compounds*, pp. 2–5, 2010.

[37] C. Longo and M.-a. D. Paoli, "Dye-Sensitized Solar Cells : A Successful Combination of Materials," *Journal Of The Brazilian Chemical Society*, vol. 14, no. 6, pp. 889–901, 2003.

[38] T. W. Hamann, R. A. Jensen, A. B. F. Martinson, H. Van Ryswyk, and J. T. Hupp, "Advancing beyond current generation dye-sensitized solar cells," *Energy and Environmental Science*, vol. 1, no. 1, p. 66, 2008.

[39] G. P. Smestad and M. Gratzel, "Demonstrating Electron Transfer and Nanotechnology: A Natural Dye-Sensitized Nanocrystalline Energy Converter," *Journal of Chemical Education*, vol. 75, p. 752, June 1998.

[40] L. M. Peter and K. G. U. Wijayantha, "Electron transport and back reaction in dye sensitised nanocrystalline photovoltaic cells," *Electrochimica Acta*, vol. 45, no. 28, pp. 4543–4551, 2000.

[41] J. Nelson and R. E. Chandler, "Random walk models of charge transfer and transport in dye sensitized systems," *Coordination Chemistry Reviews*, vol. 248, no. 13-14, pp. 1181–1194, 2004.

[42] A. Hagfeldt and M. Grätzel, "Molecular Photovoltaics," *Accounts of Chemical Research*, vol. 33, no. 5, pp. 269–277, 2000.

[43] A. M. Biswas, S. A. Haque, T. Lutz, I. Montanarh, C. Olson, R. L. Willis, J. R. Durrant, and J. Nelson, "Charge Recombination and Transport in Dye Sensitised TiO_2 Photovoltaic Devices," in *Conference Record Of The Twenty-Eighth Ieee Photovoltaic Specialists Conference -2000* (IEEE, ed.), (Anchorage, AK), pp. 796–801, IEEE, 345 E 47th ST, New York, NY 10017 USA, 2000.

[44] A. Kumar, P. G. Santangelo, and N. S. Lewis, "Electrolysis of Water at SrTiO, Photoelectrodes: Distlngulshlng between the Statistical and Stochastic Formalisms for Electron-Transfer Processes In Fuel-Formlng Photoelectrochemical Systems," *Journal Of Physical Chemistry*, vol. 96, no. 2, pp. 834–842, 1992.

[45] M. K. Nazeeruddin, A. Kay, I. Rodicio, R. Humphry-Baker, E. Miiller, P. Liska, N. Vlachopoulos, and M. Gratzel, "Conversion of Light to Elec-

tricity by cis-XzBis(2,2-bipyridyl-4,4-dicarboxylate)ruthenium(11) Charge-Transfer Sensitizers (X = C1$^-$, Br$^-$, I$^-$, CN$^-$, and SCN$^-$) on Nanocrystalline TiO_2 Electrodes," *Journal of American Chemical Society*, vol. 115, no. 4, pp. 6382–6390, 1993.

[46] H. Kusama, M. Kurashige, and H. Arakawa, "Influence of nitrogen-containing heterocyclic additives in I^-/I_3^- redox electrolytic solution on the performance of Ru-dye-sensitized nanocrystalline TiO_2 solar cell," *Journal of Photochemistry and Photobiology A: Chemistry*, vol. 169, no. 2, pp. 169–176, 2005.

[47] N. Kopidakis, N. R. Neale, and A. J. Frank, "Effect of an adsorbent on recombination and band-edge movement in dye-sensitized TiO_2 solar cells: evidence for surface passivation.," *The Journal of Physical Chemistry B*, vol. 110, pp. 12485–9, June 2006.

[48] A. Ofir, L. Grinis, and A. Zaban, "Direct Measurement of the Recombination Losses via the Transparent Conductive Substrate in Dye Sensitized Solar Cells," *Journal of Physical Chemistry C*, vol. 112, pp. 2779–2783, Feb. 2008.

[49] K. C. Mandal, A. Smirnov, D. Peramunage, and R. D. Rauh, "Low-Cost, Large-Area Nanocrystalline TiO_2 -Polymer Solar Cells on Flexible Plastics," *Materials Research*, vol. 737, pp. 1–6, 2003.

[50] C. G. Granqvist, "Transparent conductors as solar energy materials:

A panoramic review," *Solar Energy Materials and Solar Cells*, vol. 91, no. 17, pp. 1529–1598, 2007.

[51] X. Huang, P. Shen, B. Zhao, X. Feng, S. Jiang, H. Chen, H. Li, and S. Tan, "Stainless steel mesh-based flexible quasi-solid dye-sensitized solar cells," *Solar Energy Materials and Solar Cells*, pp. 1–6, 2010.

[52] J. Herrero and C. Guillen, "Transparent films on polymers for photovoltaic applications," in *7th European Vacuum Conference (EVC-7)/3rd European Topical Conference on Hard Coatings (ETCHC-3)*, (Madrid, Spain), pp. 611–616, Pergamon-Elsevier Science Ltd, 2002.

[53] Y. Soo Kim, S. Bin Oh, J. Hyeok Park, M. Suk Cho, and Y. Lee, "Highly conductive PEDOT/silicate hybrid anode for ITO-free polymer solar cells," *Solar Energy Materials and Solar Cells*, vol. 94, no. 3, pp. 471–477, 2010.

[54] G. Exarhos and X. Zhou, "Discovery-based design of transparent conducting oxide films," *Thin Solid Films*, vol. 515, no. 18, pp. 7025–7052, 2007.

[55] C. G. Granqvist and A. Hultaker, "Transparent and conducting ITO films: new developments and applications," in *2nd International Symposium on Transparent Oxide Thin Films for Electronics and Optics (TOEO-2)*, (Tokyo, Japan), pp. 1–5, Elsevier Science Sa, 2002.

[56] H. Tahar, T. Ban, Y. Ohya, and Y. Takahashi, "Tin doped indium oxide thin films : Electrical properties," *Journal of Applied Physics*, vol. 83, no. 5, 1998.

[57] G. Kalita, M. Matsushima, H. Uchida, K. Wakita, and M. Umeno, "Graphene constructed carbon thin films as transparent electrodes for solar cell applications," *Journal of Materials Chemistry*, vol. 20, no. 43, pp. 9713–9717, 2010.

[58] J.-K. Lee, B.-H. Jeong, S.-i. Jang, Y.-G. Kim, Y.-W. Jang, S.-B. Lee, and M.-R. Kim, "Preparations of TiO_2 pastes and its application to light-scattering layer for dye-sensitized solar cells," *Journal of Industrial and Engineering Chemistry*, vol. 15, no. 5, pp. 724–729, 2009.

[59] L. N. Lewis, J. L. Spivack, S. Gasaway, E. D. Williams, J. Y. Gui, V. Manivannan, and O. P. Siclovan, "A novel UV-mediated low-temperature sintering of TiO_2 for dye-sensitized solar cells," *Solar Energy Materials and Solar Cells*, vol. 90, no. 7-8, pp. 1041–1051, 2006.

[60] P. C.-y. Chen, G. Rothenberger, and M. Grätzel, "The Influence of Particle Sizes on the Optical Characteristics of Nanocrystalline TiO_2 Films for Dye-Sensitized Solar Cells," *Materials Research*, vol. 1101, p. 6, 2008.

[61] N. R. Armstrong, P. A. Veneman, E. Ratcliff, D. Placencia, and M. Brumbach, "Oxide contacts in organic photovoltaics: characterization and

control of near-surface composition in indium-tin oxide (ITO) electrodes.," *Accounts of chemical research*, vol. 42, pp. 1748–57, Nov. 2009.

[62] S. H. Keshmiri, M. Rezaee-Roknabadi, and S. Ashok, "A novel technique for increasing electron mobility of indium-tin-oxide transparent conducting films," *Thin Solid Films*, vol. 413, no. 1-2, pp. 167–170, 2002.

[63] M. Topič, A. Čampa, M. Filipič, M. Berginc, U. O. Krašovec, and F. Smole, "Optical And Electrical Modelling And Characterization Of Dye Sensitized Solar Cells," *Current Applied Physics*, 2010.

[64] A. Andersson, N. Johansson, P. Bröms, N. Yu, D. Lupo, and W. R. Salaneck, "Fluorine Tin Oxide as an Alternative to Indium Tin Oxide in Polymer LEDs," *Advanced Materials*, vol. 10, pp. 859–863, Aug. 1998.

[65] I. A. Ryzhikov, A. A. Pukhov, A. S. Il'in, N. P. Glukhova, K. N. Afanasiev, and A. S. Ryzhikov, "Anomalous temperature dependence of the conductivity of nanoporous ITO films," *Microelectronic Engineering*, vol. 69, no. 2-4, pp. 270–273, 2003.

[66] K. R. Millington, K. W. Fincher, and a. L. King, "Mordant dyes as sensitisers in dye-sensitised solar cells," *Solar Energy Materials and Solar Cells*, vol. 91, no. 17, pp. 1618–1630, 2007.

[67] D. Wei, "Dye sensitized solar cells.," *International journal of molecular sciences*, vol. 11, pp. 1103–13, Jan. 2010.

[68] X. Wang, L. Zhi, and K. Müllen, "Transparent, conductive graphene electrodes for dye-sensitized solar cells.," *Nano letters*, vol. 8, pp. 323–7, Jan. 2008.

[69] Y.-B. Tang, C.-S. Lee, J. Xu, Z.-T. Liu, Z.-H. Chen, Z. He, Y.-L. Cao, G. Yuan, H. Song, L. Chen, L. Luo, H.-M. Cheng, W.-J. Zhang, I. Bello, and S.-T. Lee, "Incorporation of graphenes in nanostructured TiO_2 films via molecular grafting for dye-sensitized solar cell application.," *ACS NANO*, vol. 4, pp. 3482–8, June 2010.

[70] S. Sun, L. Gao, and Y. Liu, "Enhanced dye-sensitized solar cell using graphene-TiO_2 photoanode prepared by heterogeneous coagulation," *Applied Physics Letters*, vol. 96, no. 8, p. 083113, 2010.

[71] B. S. Kim, D. H. Lee, S. H. Kim, G. H. An, K. J. Lee, N. V. Myung, and Y. H. Choa, "Silicon Solar Cell with Nanoporous Structure Formed on a Textured Surface," *Journal of the American Ceramic Society*, vol. 92, no. 10, pp. 2415–2417, 2009.

[72] H. Choi, H. Kim, S. Hwang, M. Kang, D.-W. Jung, and M. Jeon, "Electrochemical electrodes of graphene-based carbon nanotubes grown by chemical vapor deposition," *Scripta Materialia*, pp. 27–30, Nov. 2010.

[73] A. S. Barnard and H. Xu, "An environmentally sensitive phase map of titania nanocrystals.," *ACS nano*, vol. 2, pp. 2237–42, Nov. 2008.

[74] Solaronix, "Dye Solar Cell: Assembly Instructions," 2010.

[75] B. Koo, J. Park, Y. Kim, S.-H. Choi, Y.-E. Sung, and T. Hyeon, "Simultaneous phase- and size-controlled synthesis of TiO_2 nanorods via non-hydrolytic sol-gel reaction of syringe pump delivered precursors.," *The Journal of Physical Chemistry B*, vol. 110, pp. 24318–23, Dec. 2006.

[76] K. Shankar, G. K. Mor, H. E. Prakasam, O. K. Varghese, and C. A. Grimes, "Self-assembled hybrid polymer-TiO_2 nanotube array heterojunction solar cells," *Langmuir*, vol. 23, no. 24, pp. 12445–12449, 2007.

[77] K. Shankar, J. I. Basham, N. K. Allam, O. K. Varghese, G. K. Mor, X. Feng, M. Paulose, J. A. Seabold, K.-S. Choi, and C. A. Grimes, "Recent Advances in the Use of TiO_2 Nanotube and Nanowire Arrays for Oxidative Photoelectrochemistry," *The Journal of Physical Chemistry C*, vol. 113, no. 16, pp. 6327–6359, 2009.

[78] B. Tan and Y. Y. Wu, "Dye-sensitized solar cells based on anatase TiO_2 nanoparticle/nanowire composites," *Journal of Physical Chemistry B*, vol. 110, no. 32, pp. 15932–15938, 2006.

[79] H. Xu, X. Tao, D.-T. Wang, Y.-Z. Zheng, and J.-F. Chen, "Enhanced efficiency in dye-sensitized solar cells based on TiO_2 nanocrystal/nanotube double-layered films," *Electrochimica Acta*, vol. 55, no. 7, pp. 2280–2285, 2010.

[80] H. Nishikiori, Y. Uesugi, N. Tanaka, and T. Fujii, "Photo-electric conversion in dye-doped nanocrystalline titania films," *Journal of Photo-*

chemistry and Photobiology A: Chemistry, vol. 207, no. 2-3, pp. 204–208, 2009.

[81] R. Chandrasekar, L. F. Zhang, J. Y. Howe, N. E. Hedin, Y. Zhang, and H. Fong, "Fabrication and characterization of electrospun titania nanofibers," *Journal of Materials Science*, vol. 44, no. 5, pp. 1198–1205, 2009.

[82] K. Fujihara, A. Kumar, R. Jose, S. Ramakrishna, and S. Uchida, "Spray deposition of electrospun TiO_2 nanorods for dye-sensitized solar cell," *Nanotechnology*, vol. 18, no. 36, 2007.

[83] S. H. Lee, C. Tekmen, and W. M. Sigmund, "Three-point bending of electrospun TiO_2 nanofibers," *Materials Science and Engineering A-Structural Materials Properties Microstructure and Processing*, vol. 398, no. 1-2, pp. 77–81, 2005.

[84] N.-g. Park, S.-h. Chang, J. V. D. Lagemaat, K.-j. Kim, and A. J. Frank, "Effect of Cations on the Open-Circuit Photovoltage and the Charge-Injection Efficiency of Dye-Sensitized Nanocrystalline Rutile TiO_2 Films," *Bulletin of the Korean Chemical Society*, vol. 21, no. 10, pp. 985–988, 2000.

[85] Y. F. Zhu, L. Zhang, C. Gao, and L. L. Cao, "The synthesis of nano-sized TiO_2 powder using a sol-gel method with $TiCl_4$ as a precursor," *JOURNAL OF MATERIALS SCIENCE*, vol. 35, no. 16, pp. 4049–4054, 2000.

[86] W. Payakgul, O. Mekasuwandumrong, V. Pavarajarn, and N. P. Praserthdam, "Effects of reaction medium on the synthesis of TiO_2 nanocrystals by thermal decomposition of titanium (IV) n-butoxide," *CERAMICS INTERNATIONAL*, vol. 31, no. 3, pp. 391–397, 2005.

[87] J. Deitzel, "The effect of processing variables on the morphology of electrospun nanofibers and textiles," *Polymer*, vol. 42, pp. 261–272, Jan. 2001.

[88] M. Demir, I. Yilgor, E. Yilgor, and B. Erman, "Electrospinning of polyurethane fibers," *Polymer*, vol. 43, pp. 3303–3309, May 2002.

[89] R. Dersch, T. Liu, A. K. Schaper, A. Greiner, and J. H. Wendorff, "Electrospun Nanofibers : Internal Structure and Intrinsic," *Journal of Polymer Science Part A: Polymer Chemistry*, vol. 41, pp. 545–553, 2002.

[90] Z. Huang, "A review on polymer nanofibers by electrospinning and their applications in nanocomposites," *Composites Science and Technology*, vol. 63, no. 15, pp. 2223–2253, 2003.

[91] K. Onozuka, B. Ding, Y. Tsuge, T. Naka, M. Yamazaki, S. Sugi, S. Ohno, M. Yoshikawa, and S. Shiratori, "Electrospinning processed nanofibrous TiO_2 membranes for photovoltaic applications," *Nanotechnology*, vol. 17, no. 4, pp. 1026–1031, 2006.

[92] M. Y. Song, D. K. Kim, K. J. Ihn, S. M. Jo, and D. Y. Kim, "New application of electrospun TiO_2 solid-state dye-sensitized solar electrode

to cells," in *Synthetic Metals*, pp. 77–80, 2005.

[93] S. M. Jo, M. Y. Song, Y. R. Ahn, C. R. Park, and D. Y. Kim, "Nanofibril formation of electrospun TiO_2 fibers and its application to dye-sensitized solar cells," *Journal of Macromolecular Science, Part A: Pure and Applied Chemistry*, vol. A42, no. 11, pp. 1529–1540, 2005.

[94] T. Y. Lee, P. S. Alegaonkar, and J.-B. Yoo, "Fabrication of dye sensitized solar cell using TiO_2 coated carbon nanotubes," *Thin Solid Films*, vol. 515, no. 12, pp. 5131–5135, 2007.

[95] K. Lee, C. Hu, H. Chen, and K. Ho, "Incorporating carbon nanotube in a low-temperature fabrication process for dye-sensitized TiO2 solar cells," *Solar Energy Materials and Solar Cells*, vol. 92, no. 12, pp. 1628–1633, 2008.

[96] T. Sawatsuk, A. Chindaduang, C. Sae-Kung, S. Pratontep, and G. Tumcharern, "Dye-sensitized solar cells based on TiO_2-MWCNTs composite electrodes: Performance improvement and their mechanisms," *Diamond and Related Materials*, vol. 18, pp. 524–527, 2009.

[97] A. Kay and M. Graetzel, "Artificial photosynthesis. 1. Photosensitization of titania solar cells with chlorophyll derivatives and related natural porphyrins," *The Journal of Physical Chemistry*, vol. 97, pp. 6272–6277, June 1993.

[98] S. Hao, J. Wu, Y. Huang, and J. Lin, "Natural dyes as photosensitizers for dye-sensitized solar cell," *Solar Energy*, vol. 80, no. 2, pp. 209–214, 2006.

[99] K. Wongcharee, V. Meeyoo, and S. Chavadej, "Dye-sensitized solar cell using natural dyes extracted from rosella and blue pea flowers," *Solar Energy Materials and Solar Cells*, vol. 91, no. 7, pp. 566–571, 2007.

[100] N. M. Gómez-Ortíz, I. A. Vázquez-Maldonado, A. R. Pérez-Espadas, G. J. Mena-Rejón, J. A. Azamar-Barrios, and G. Oskam, "Dye-sensitized solar cells with natural dyes extracted from achiote seeds," *Solar Energy Materials and Solar Cells*, vol. 94, no. 1, pp. 40–44, 2009.

[101] E. Yamazaki, M. Murayama, N. Nishikawa, N. Hashimoto, M. Shoyama, and O. Kurita, "Utilization of natural carotenoids as photosensitizers for dye-sensitized solar cells," *Solar Energy*, vol. 81, no. 4, pp. 512–516, 2007.

[102] N. J. Cherepy, G. P. Smestad, M. Grätzel, and J. Z. Zhang, "Ultrafast Electron Injection: Implications for a Photoelectrochemical Cell Utilizing an Anthocyanin Dye-Sensitized TiO_2 Nanocrystalline Electrode," *The Journal of Physical Chemistry B*, vol. 101, pp. 9342–9351, Nov. 1997.

[103] H. J. Snaith and L. Schmidt-Mende, "Advances in liquid-electrolyte and solid-state dye-sensitized solar cells," *Advanced Materials*, vol. 19, no. 20, pp. 3187–3200, 2007.

[104] A. Hauch, "Diffusion in the electrolyte and charge-transfer reaction at the platinum electrode in dye-sensitized solar cells," *Electrochimica Acta*, vol. 46, pp. 3457–3466, Aug. 2001.

[105] P. M. Sommeling, H. C. Rieffe, J. A. M. van Roosmalen, A. Schönecker, J. M. Kroon, J. A. Wienke, and A. Hinsch, "Spectral response and IV-characterization of dye-sensitized nanocrystalline TiO_2 solar cells," *Solar Energy Materials and Solar Cells*, vol. 62, no. 4, pp. 399–410, 2000.

[106] K. Hara, T. Nishikawa, M. Kurashige, H. Kawauchi, T. Kashima, K. Sayama, K. Alka, and H. Arakawa, "Influence of electrolyte on the photovoltaic performance of a dye-sensitized TiO_2 solar cell based on a Ru(II) terpyridyl complex photosensitizer," *Solar Energy Materials and Solar Cells*, vol. 85, no. 1, pp. 21–30, 2005.

[107] S. A. Cerneaux, S. M. Zakeeruddin, M. Grätzel, Y.-B. Cheng, and L. Spiccia, "New functional triethoxysilanes as iodide sources for dye-sensitized solar cells," *Journal of Photochemistry and Photobiology A: Chemistry*, vol. 198, no. 2-3, pp. 186–191, 2008.

[108] H. Olivier-Bourbigou, L. Magna, and D. Morvan, "Ionic liquids and catalysis: Recent progress from knowledge to applications," *Applied Catalysis A: General*, vol. 373, no. 1-2, pp. 1–56, 2010.

[109] U. Opara Krasovec, M. Berginc, M. Hocevar, and M. Topic, "Unique TiO_2 paste for high efficiency dye-sensitized solar cells," *Solar Energy Materials and Solar Cells*, vol. 93, no. 3, pp. 379–381, 2009.

[110] T. N. Murakami and M. Gratzel, "Counter electrodes for DSC: Application of functional materials as catalysts," *Inorganica Chimica Acta*, vol. 361, no. 3, pp. 572–580, 2008.

[111] M. Biancardo, K. West, and F. C. Krebs, "Quasi-solid-state dye-sensitized solar cells: Pt and PEDOT:PSS counter electrodes applied to gel electrolyte assemblies," *Journal of Photochemistry and Photobiology A: Chemistry*, vol. 187, no. 2-3, pp. 395–401, 2007.

[112] K.-M. Lee, W.-H. Chiu, H.-Y. Wei, C.-W. Hu, V. Suryanarayanan, W.-F. Hsieh, and K.-C. Ho, "Effects of mesoscopic poly(3,4-ethylenedioxythiophene) films as counter electrodes for dye-sensitized solar cells," *Thin Solid Films*, vol. 518, no. 6, pp. 1716–1721, 2010.

[113] M. Toivola, F. Ahlskog, and P. Lund, "Industrial sheet metals for nanocrystalline dye-sensitized solar cell structures," *Solar Energy Materials and Solar Cells*, vol. 90, no. 17, pp. 2881–2893, 2006.

[114] G. Calogero, F. Bonaccorso, O. M. Maragò, P. G. Gucciardi, and G. Di Marco, "Single wall carbon nanotubes deposited on stainless steel sheet substrates as novel counter electrodes for ruthenium polypyridine based dye sensitized solar cells.," *Dalton transactions (Cambridge, England : 2003)*, vol. 39, no. 11, pp. 2903–9, 2010.

[115] T. Hino, Y. Ogawa, and N. Kuramoto, "Dye-Sensitized Solar Cell with Single Walled Carbon Nanotube Thin Film Prepared by an Electrolytic

Micelle Disruption Method as the Counterelectrode," *Fullerenes, Nanotubes, and Carbon Nanostructures*, vol. 14, no. 4, pp. 607–619, 2006.

[116] D. B. Kuang, P. Wang, S. Ito, S. M. Zakeeruddin, and M. Gratzel, "Stable mesoscopic dye-sensitized solar cells based on tetracyanoborate ionic liquid electrolyte," *Journal of the American Chemical Society*, vol. 128, no. 24, pp. 7732–7733, 2006.

[117] N. Papageorgiou, Y. Athanassov, M. Armand, P. Bonhote, H. Pettersson, A. Azam, and M. Gratzel, "The performance and stability of ambient temperature molten salts for solar cell applications," *Journal of The Electrochemical Society*, vol. 143, no. 10, pp. 3099–3108, 1996.

[118] G. Boschloo, L. Häggman, and A. Hagfeldt, "Quantification of the effect of 4-tert-butylpyridine addition to I^-/I_3^- redox electrolytes in dye-sensitized nanostructured TiO_2 solar cells.," *Journal of Physical Chemistry B*, vol. 110, pp. 13144–50, July 2006.

[119] J. Villanueva, J. a. Anta, E. Guillen, and G. Oskam, "Numerical Simulation of the CurrentVoltage Curve in Dye-Sensitized Solar Cells," *The Journal of Physical Chemistry C*, vol. 113, pp. 19722–19731, Nov. 2009.

[120] N. Kopidakis, K. D. Benkstein, J. van De Lagemaat, and A. J. Frank, "Transport-Limited Recombination of Photocarriers in Dye-Sensitized Nanocrystalline TiO_2 Solar Cells," *The Journal of Physical Chemistry B*, vol. 107, pp. 11307–11315, Oct. 2003.

[121] S. Södergren, A. Hagfeldt, and S.-e. Lindquist, "Theoretical Models for the Action Spectrum and the Current-Voltage Characteristics of Microporous Semiconductor Films in Photoelectrochemical Cells," *Journal of physical Chemistry*, vol. 98, no. 21, pp. 5552–5556, 1994.

[122] R. Gomez and P. Salvador, "Photovoltage dependence on film thickness and type of illumination in nanoporous thin film electrodes according to a simple diffusion model," *Solar Energy Materials and Solar Cells*, vol. 88, pp. 377–388, Sept. 2005.

[123] M. Ni, M. Leung, D. Leung, and K. Sumathy, "Theoretical modeling of TiO_2/TCO interfacial effect on dye-sensitized solar cell performance," *Solar Energy Materials and Solar Cells*, vol. 90, pp. 2000–2009, Aug. 2006.

[124] G. Kron, T. Egerter, J. H. Werner, and U. Rau, "Electronic transport in dye-sensitized nanoporous TiO_2 solar cells - Comparison of electrolyte and solid-state devices," *Journal of Physical Chemistry B*, vol. 107, no. 15, pp. 3556–3564, 2003.

[125] A. Fischer, H. Pettersson, A. Hagfeldt, G. Boschloo, L. Kloo, and M. Gorlov, "Crystal formation involving 1-methylbenzimidazole in iodide/triiodide electrolytes for dye-sensitized solar cells," *Solar Energy Materials and Solar Cells*, vol. 91, no. 12, pp. 1062–1065, 2007.

[126] O. K. Varghese and C. A. Grimes, "Appropriate strategies for determining the photoconversion efficiency of water photo electrolysis cells: A

review with examples using titania nanotube array photoanodes," *Solar Energy Materials and Solar Cells*, vol. 92, no. 4, pp. 374–384, 2008.

[127] K. Ocakoglu, F. Yakuphanoglu, J. R. Durrant, and S. Icli, "The effect of temperature on the charge transport and transient absorption properties of K27 sensitized DSSC," *Solar Energy Materials and Solar Cells*, vol. 92, no. 9, pp. 1047–1053, 2008.

[128] H. J. Snaith, L. Schmidt-Mende, M. Gratzel, and M. Chiesa, "Light intensity, temperature, and thickness dependence of the open-circuit voltage in solid-state dye-sensitized solar cells," *Physical Review B*, vol. 74, no. 4, p. 6, 2006.

[129] P. J. Sebastian, A. Olea, J. Campos, J. A. Toledo, and S. A. Gamboa, "Temperature dependence and the oscillatory behavior of the optoelectronic properties of a dye-sensitized nanocrystalline TiO_2 solar cell," *Solar Energy Materials and Solar Cells*, vol. 81, no. 3, pp. 349–361, 2004.

[130] A. Royne, C. J. Dey, and D. R. Mills, "Cooling of photovoltaic cells under concentrated illumination: a critical review," *Solar Energy Materials and Solar Cells*, vol. 86, no. 4, pp. 451–483, 2005.

[131] M. Dufek, *The Quanta FEG User Operation Manual.* FEI Company, 3 ed., Oct. 2007.

Vita

Edwin Peng was born in Monterey Park, California on November 12, 1989, the son of Vincent Peng and Norma Peng. At the age of 13, he was enrolled as a full time student at California State University, Los Angeles (CSULA) through the Early Entrance Program. He served in the CSULA student government as the Community Affairs Representative, a member of the student government's Executive Committee, and the Student Representative on the Faculty Policy Committee of the CSULA Academic Senate. He also was the President of the CSULA Student Section of the American Society of Mechanical Engineers and became a member of Tau Beta Pi and Pi Tau Sigma. Edwin Peng graduated from CSULA with a Bachelor of Science in mechanical engineering in 2008. He was admitted into the Graduate School at The University of Texas at Austin (UT) in 2009. He is currently a graduate research assistant at the Solar Energy and Biofuels Laboratory in UT.

Permanent address: 3401 Red River Street #127
Austin, Texas 78705

This thesis was typeset with LaTeX[†] by the author.

[†]LaTeX is a document preparation system developed by Leslie Lamport as a special version of Donald Knuth's TeX Program.